Title
Multisource X-ray Systems for Digital Breast Tomosynthesis and Breast CT Imaging

Author
Becker, Amy Elizabeth

Publication Date
2021

Peer reviewed|Thesis/dissertation

Multisource X-ray Systems for Digital Breast Tomosynthesis and Breast CT Imaging

By

AMY ELIZABETH BECKER
DISSERTATION

Submitted in partial satisfaction of the requirements for the degree of

DOCTOR OF PHILOSOPHY

in

Biomedical Engineering

in the

OFFICE OF GRADUATE STUDIES

of the

UNIVERSITY OF CALIFORNIA

DAVIS

Approved:

_____
John Boone, Chair

_____
Ramsey Badawi

_____
Anthony Seibert

Committee in Charge

2021

To Susan Becker, my mom

“Vulnerability is not knowing victory or defeat, it’s understanding the necessity of both; it’s engaging. It’s being all in.” -Brené Brown

Acknowledgements

I am grateful for the support from my family that gave me the emotional, intellectual, and financial foundation to pursue my goals as well as my mom for inspiring my focus on breast cancer research. My father, Michael Becker, has been my greatest support and I cherish our relationship and how our family has grown with my stepmother Judy Glasser. The love from my family shaped my core identity which allows me to build healthy relationships that foster my professional success.

Thank you to my PhD advisor Dr. John Boone for welcoming me into his lab space and advocating for my career development. I appreciate the freedom that you gave me to travel to conferences, build my network, and learn by trial and error. I am grateful for the experience to support the clinical trial and various research projects in the lab. Thank you to Dr. Andrew Hernandez for his dedication to this work and attention to detail in the pursuit of great science. Thank you to Sunny Lyu and Janani Aiyer for bringing new perspectives and enthusiasm for the projects, learning together with you motivated me to finish my PhD. Thank you to George Burkett for being a reliable labmate and good friend.

Thank you to our collaborator Dr. Paul Schwoebel at University of New Mexico for the expertise that enabled us to realize the MXA technology. Thank you to our collaborator Dr. Craig Abbey at University of California, Santa Barbara for the expertise in model observer studies that that gave us the tools to complete the microcalcification detectability calculations. Thank you to Dr. Ramsey Badawi and Dr. Anthony Seibert for serving on my dissertation committee and Dr. Guobao Wang for serving on my qualifying exam committee for the valuable feedback and support throughout graduate school. I also appreciate the encouragement and feedback from faculty in the UC Davis Radiology research group including Dr. Emilie Roncali, Dr. Simon Cherry, Dr. Abhijit Chaudhari, and Dr. Audrey Fan.

Thank you to my new friends in California who encouraged exploration in this new place. Moving away from my family in pursuit of this degree was challenging in many ways, but my friends and the community in the Biomedical Engineering Student Association gave me a new foundation here. I learned about myself and what is most valuable for me in my professional and personal relationships. Thank you to my best friend Emily Misnick for pushing me to be a better person and see the world with new perspectives. Finally thank you to Janice Adams and her family who supported me during the COVID-19 pandemic and her two lovely cats who brought me joy during quarantine!

Abstract

This dissertation is focused on the development and characterization of a novel x-ray tube prototype for digital breast tomosynthesis (DBT) and the application of this multisource approach to cone beam CT (CBCT) and dedicated breast CT (bCT). The design and testing of a prototype Multi-X-ray-source Array (MXA) for DBT is reported. The MXA is comprised of an array of tungsten filament cathodes with focus cup grid-controlled modulation and a common rotating anode housed in a single vacuum envelope. Prototypes consisting of arrays of three-source elements and eleven-source-elements were fabricated and evaluated. The prototype sources demonstrated focal spot sizes of 0.3 mm at 45 kV with 50 mA. Measured X-ray spectra were consistent with the molybdenum anode employed, and the tube output (air kerma) was between 0.6 mGy/100 mAs at 20 kV and 17 mGy/100 mAs at 45 kV with a distance of 100 cm. HVL measurements ranged from 0.5 mm Al at 30 kV to 0.8 mm Al at 45 kV, and X-ray pulse widths were varied from 20 ms to 110 ms at operating frequencies ultimately to be limited by source turn-on/off times of ~1 ms. Initial results of reconstructed tomographic data were presented.

Multisource configurations were applied to CBCT using phantom imaging and Monte Carlo simulations. Image quality, scatter, and dose were evaluated in both overlapping (large cone angle) and collimated (small cone angle) configurations for CBCT. Four x-ray tube configurations were considered: traditional one source, three source overlapping, six source overlapping, and six sources collimated. Image quality was evaluated on a prototype breast CT system using the following five phantoms: a Defrise phantom, a previously reported CBCT QA phantom (Corgi), a polyethylene cylinder, and two anthropomorphic phantoms (hand and knee). Scatter contamination and radiation dose were evaluated using Monte Carlo simulations of a voxelized polyethylene cylinder.

The modulation of the Defrise phantom disks on average was 2.7X greater for the six-source collimated configuration than the six-source overlapping configuration. The data lost from cone beam artifact (spatial domain) and the null cone (frequency domain) in the overlapping configuration were completely recovered using the collimated configuration. The maximum scatter to primary ratio (SPR) for the overlapping configuration was 0.81 and the maximum SPR for the collimated configuration was 0.26. The average dose and maximum dose was 4X less in the collimated six source configuration when compared with the overlapping configurations. The maximum dose for the overlapping configurations (one, three & six) remained constant, but the average dose for the multisource (three & six source) overlapping configurations increased 25% when compared to the one source configuration. Use of a collimated multisource x-ray tube configuration was shown to provide significant improvements in image quality throughout the cone-beam geometry field-of-view, reduction in scatter contamination, and more efficient use of dose in comparison to both traditional cone-beam CT geometry with a single source and the overlapping multisource configurations.

A phantom was developed to simulate microcalcification lesions and a non-prewhitening-matched filter (NPW) model was applied to evaluate detectability for various technique parameters and cone angle regions in bCT. The detectability of microcalcifications was improved with smaller pixel size (75 μm) and higher dose (6 mGy) when compared to larger pixel size (150 μm) and lower dose (3 mGy). The number of projections (N = 250 or N = 500) did not affect the detectability significantly. The detectability decreased from small to medium cone angle regions and from small to large cone angle regions but was not significantly affected from medium to large cone angle regions. The differences in detectability across cone angle regions was more prominent in the coronal plane than the sagittal and axial planes.

Table of Contents

Chapter 1: Background

1.1. Breast cancer screening

The American Cancer Society predicts that 1 in 8 women will get breast cancer during their lifetime[1]. Breast cancer is the second leading cause of cancer death in women, and the rate of survival is highly dependent on the stage of detection. Digital mammography (DM) is the standard technique for breast screening in the normal risk population, but still 1 in 6 cancers are missed on average using this technique[2]. This has led to the investigation of tomographic x-ray imaging techniques such as digital breast tomosynthesis (DBT) and dedicated breast CT (bCT) to overcome the limitations of DM.

Digital mammography (DM) produces 2D images of a 3D object, leading to the superposition of tissues and a high false positive rate. Breast MRI is used for screening high risk populations but is not suitable for the normal risk population because it uses contrast injection which is more invasive, and it is more expensive and time consuming. Ultrasound imaging is most often used to investigate lesions after they are detected and sometimes with automated breast ultrasound scanning (ABUS), which results in many images for the radiologist to sift though.

Digital breast tomosynthesis (DBT) and dedicated breast CT (bCT) are x-ray imaging techniques that both aim to overcome the superposition of tissues in DM by collecting images around the breast and reconstructing them into a volume dataset. DBT is a modified version of digital mammography, with a rotating x-ray tube that collects several projection images (11-49) of the compressed breast over a limited angle range (15-50°). Dedicated bCT is a specialized geometry of cone beam CT that collects 300-500 projections in a complete rotation (360°) around the pendant (uncompressed) breast. The projection images in DBT are used to reconstruct a

pseudo-3D volume dataset of image slices, while the projection images in bCT are reconstructed into a true 3D volume dataset. There are several DBT scanners and one dedicated bCT scanner that is FDA approved. DM and DBT both use compression of the breast between two plates, which is uncomfortable for the patient and can deter women from returning for regular screenings. Dedicated bCT does not use breast compression, therefore it is more comfortable and has the potential to increase screening compliance.

Breast cancer lesions are generally categorized as either masses or microcalcifications, and both are important for breast cancer screening. Masses are low contrast larger soft tissue lesions and microcalcifications are high contrast small calcium deposits. Since they are structurally different, it is challenging to optimize one imaging protocol that will maximize the visibility of both lesion types. The generation of volume datasets in bCT and DBT overcomes the anatomical noise caused by superposition of tissues in DM, but the volume datasets contain more noise than DM and the longer scan times enable patient motion artifacts. A comparison of parameters including number of projections, exposure per projection, pixel size, and slice separation is reported in Table 1.1.

Table 1.1 Summary of the relevant parameters in digital mammography, digital breast tomosynthesis, and dedicated breast CT systems that account for the tradeoffs in spatial resolution and noise levels.

Parameter per breast	FDA Approved DM	FDA Approved DBT	UC Davis Breast CT
# projections	2	9 - 25	500
mAs / projection	50	4 - 11	0.35
x-y pixel size [mm]	0.07	0.07	0.15
slice separation [mm]	-	1.00	0.15

1.2. Multisource x-ray systems

The use of multiple x-ray sources in medical imaging systems that produce tomographic data is of interest for reasons ranging from reducing or eliminating mechanical motion to decreasing image acquisition times and system costs. The various approaches and their history have been thoroughly reviewed,[3] so a summary is provided here which captures the key aspects as they relate to the technology underlying the multi-x-ray source array (MXA).

Beginning in the 1980's the earliest and most direct approach to incorporating multiple x-ray sources in imaging systems was implemented by the use of multiple conventional, rotating anode x-ray tubes, and such designs are commercially available today.[4] About this same time sophisticated systems were developed in which an electron beam was scanned over a spatially distributed target to produce an x-ray source that moved through space without mechanical motion, creating a "stationary" x-ray source[5]. Subsequent approaches to multiple x-ray source systems grew to include the use of arrays of discrete, addressable cathodes distributed in space, often within a single vacuum envelope and referred to as 'distributed x-ray sources'. The cathodes used in distributed x-ray sources include thermionic cathodes[6] (tungsten filaments, dispenser, and oxide) and field electron emission cathodes (cold-cathodes)[7]. This work has continued with arrays of cathodes being used to produce distributed x-ray sources for CT[7,8] and stationary x-ray sources for digital breast tomosynthesis (DBT)[9]. For applications in CT, this source development has focused on the use of thermionic cathodes due to their proven performance and generally robust characteristics. Over the last decade the development of stationary sources for DBT has focused on the use of field electron emission cathode-based systems due to attractive features such as their operation at room temperature. However in the case of field emission cathodes, unfortunately, despite efforts that started nearly 100 years ago[10] and subsequent support by large financial

investments from both industry and government in the US and abroad, no commercially available medical imaging system using field emission cathodes is used routinely in a clinical setting, principally due to their poor reliability in the x-ray tube environment[11].

One common feature of distributed x-ray source systems that was reported in the scientific literature employed stationary anodes. X-ray tube anodes have inherent limitations to the sustained x-ray flux per source element they can support due to target heating considerations[12]. In principle distributed x-ray source systems can employ enough individual source elements such that anode power densities per source element are acceptable for a stationary anode. However, for tomographic imaging applications like DBT and CT, as the number of source elements is increased, the detector frame rate can become the rate-limiting step with respect to acquisition (scan) time. This can lead to systems with scan times that are too long to be clinically relevant.

The other approach to increase the sustainable flux per source element is to use a rotating anode. Rotating anodes first became commercially available[12] in the late 1920's reflecting the need to increase the sustained output of bremsstrahlung x-ray tubes by distributing the electron beam power density over a larger anode surface area. A rotating anode can easily provide, for a given exposure time, ten-times the x-ray output of a stationary anode. Although the use of rotating anodes in distributed x-ray source systems has been proposed theoretically[3] and in the patent literature, there appears to be no published research in which a rotating anode-based distributed x-ray source has been investigated before this investigation[13,14,15,16]. This dissertation will report on the initial prototype development and characterization of a novel multi-x ray-source array (MXA).

1.3. Cone beam CT systems

Cone beam CT (CBCT) was originally developed in 1982 for angiography[17], but it was not until the late 1990s that advancements in flat panel detectors (FPD) and computer technology made it possible to produce CBCT systems for routine clinical use. In the last 20 years, clinical use and continued research in CBCT has expanded its application to include angiography[18], oral and maxillofacial imaging[19], interventional radiology[20], image guided radiotheraphy[21], musculoskeletal imaging[22] and breast imaging[23,24]. The main benefits of CBCT over traditional multi-detector CT (MDCT) are higher spatial resolution with reduced cost, dose, and space requirements[22]. This has greatly increased accessibility to CT imaging for both researchers and clinicians and has allowed unique geometries to be designed for specialized applications. Conventional CBCT scanners expose the patient extremity with a cone shaped x-ray beam that covers the entire object. Projection data is collected on a flat panel detector (FPD) with a typically circular trajectory and that data is reconstructed into a 3D volume dataset. This dissertation will investigate the application of a multisource x-ray system in various configurations for cone beam CT using quantitative and qualitative analysis.

1.4. Mathematical observers

The performance of an imaging system depends on both the ability of the system to portray the necessary signal and the degree to which the clinician perceives that information for the clinical task[25]. The most common method for evaluating diagnostic image quality for a clinical task is through visual observation of phantom or patient images. When optimizing the scan technique over many parameters, it is not practical to use human observers to review the many datasets. It is more practical to apply mathematical observers[26] based on statistical decision theory to evaluate

the ability of the system to portray the necessary signal, which often correlates with human observation[27]. This dissertation will report on the development of a specialized breast phantom to evaluate the detection of microcalcifications in bCT for various technique parameters as well as comparisons across regions and planes within the field of view.

Chapter 2: Prototype Multi-X-ray-source Array (MXA) for digital breast tomosynthesis

2.1. Introduction

In this chapter we discuss a prototype multi-x-ray-source array (MXA) system as a stationary x-ray source for DBT. The MXA employs tungsten filament-type cathodes for reliability, focus-cup grid control for modulation of the individual source elements, and a rotating anode to significantly increase the sustained x-ray flux per source element over that which can be achieved with stationary anodes. Besides the elimination of any possible image blurring effects due to x-ray tube movement or vibration inherent to a stationary source,[28,29] the associated simplified system design and reduction in system size has the potential to increase reliability and decrease capital, operating, and maintenance costs. In addition, the lack of mechanical motion associated with moving the x-ray source through space combined with the use of a rotating anode to increase the sustainable x-ray flux per source element imparts the potential to significantly reduce scan times relative to proposed[9] or existing[28] commercial systems. Scan time is one of the most important parameters of a DBT system[30,31] with short scan times helping to minimize instances of image blurring due to patient motion.

2.2. Methods

2.2.1. Source design and fabrication

The MXA uses an array of tungsten filament cathodes opposing a cylindrically symmetric, rotating anode. Grid-controlled cinefluoroscopic-type-tube cathode modulation is employed to define the beam spot (i.e., x-ray focal spot) size on the anode and allow for the individual x-ray source

elements to be turned on and off. Figure 2.1 illustrates the rotating anode based MXA source concept for DBT and Figure 2.2 illustrates the breast tissue within the field of view. In a clinical DBT setting, the x-ray beam coverage would be restricted to the breast tissue with a half beam geometry designed to avoid the lungs. No collimation was used for our prototyping experiments because the source was operated in an unoccupied room. Tungsten filament cathodes were chosen

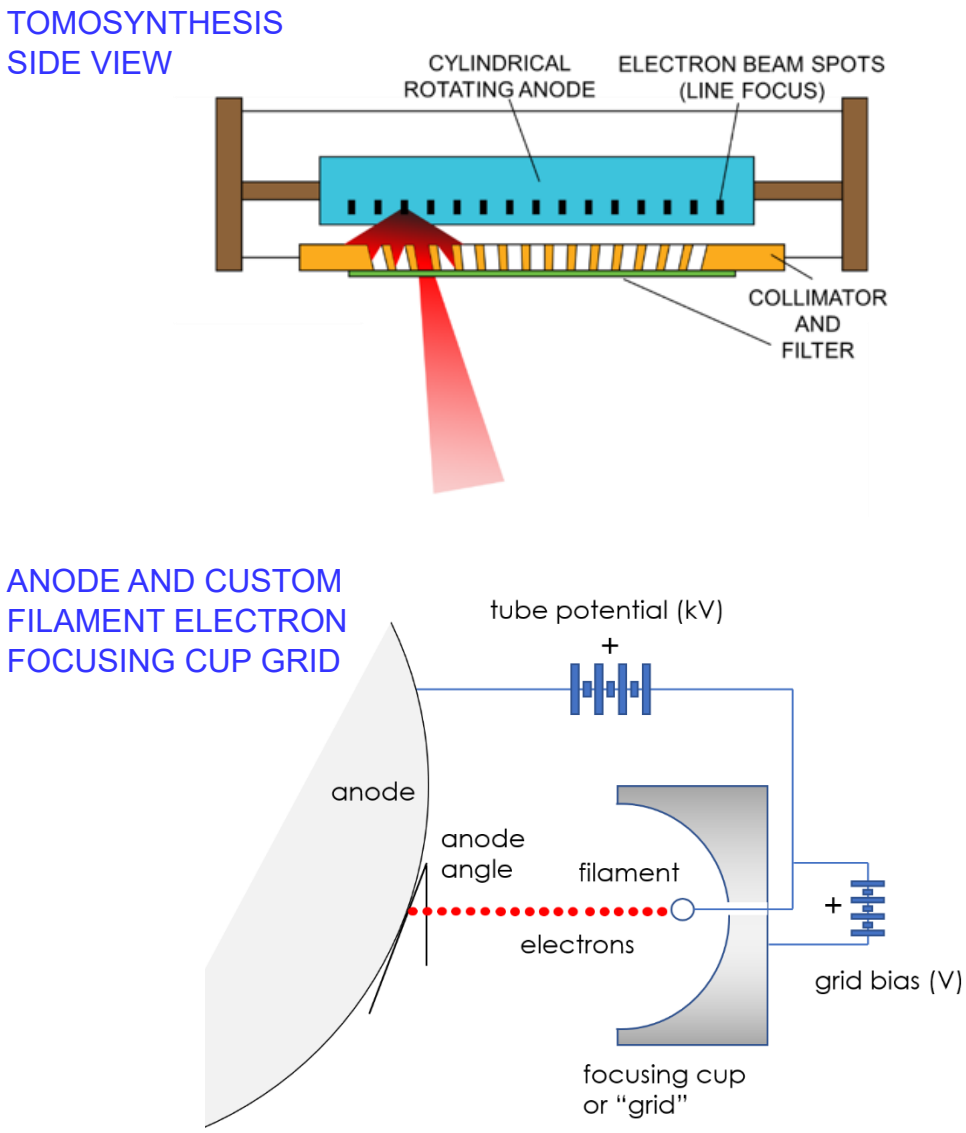

Figure 2.1. Schematic of the multi-x-ray-source array (MXA) with rotating anode assembly as applied to tomosynthesis and a close look at the custom filament and focusing cup.

due to their simple robust nature. For DBT, a stationary source replicating projection image positions of existing commercial systems requires: 1) Source densities of no greater than 1 source per degree of scan angle, equivalent to a linear power density of ~ (24 W/filament) x (1 filament/2 cm) = 12 W/cm with a total power of 15 projections x (24 W/projection) = 360 W (Hologic Dimensions 3D) and 2) and total power of less than 25 projections at 25 W = 600 W at a linear power density of ~ (24 W/projection) x (1 filament/4 cm) = 8 W/cm (Siemens Mammomat with

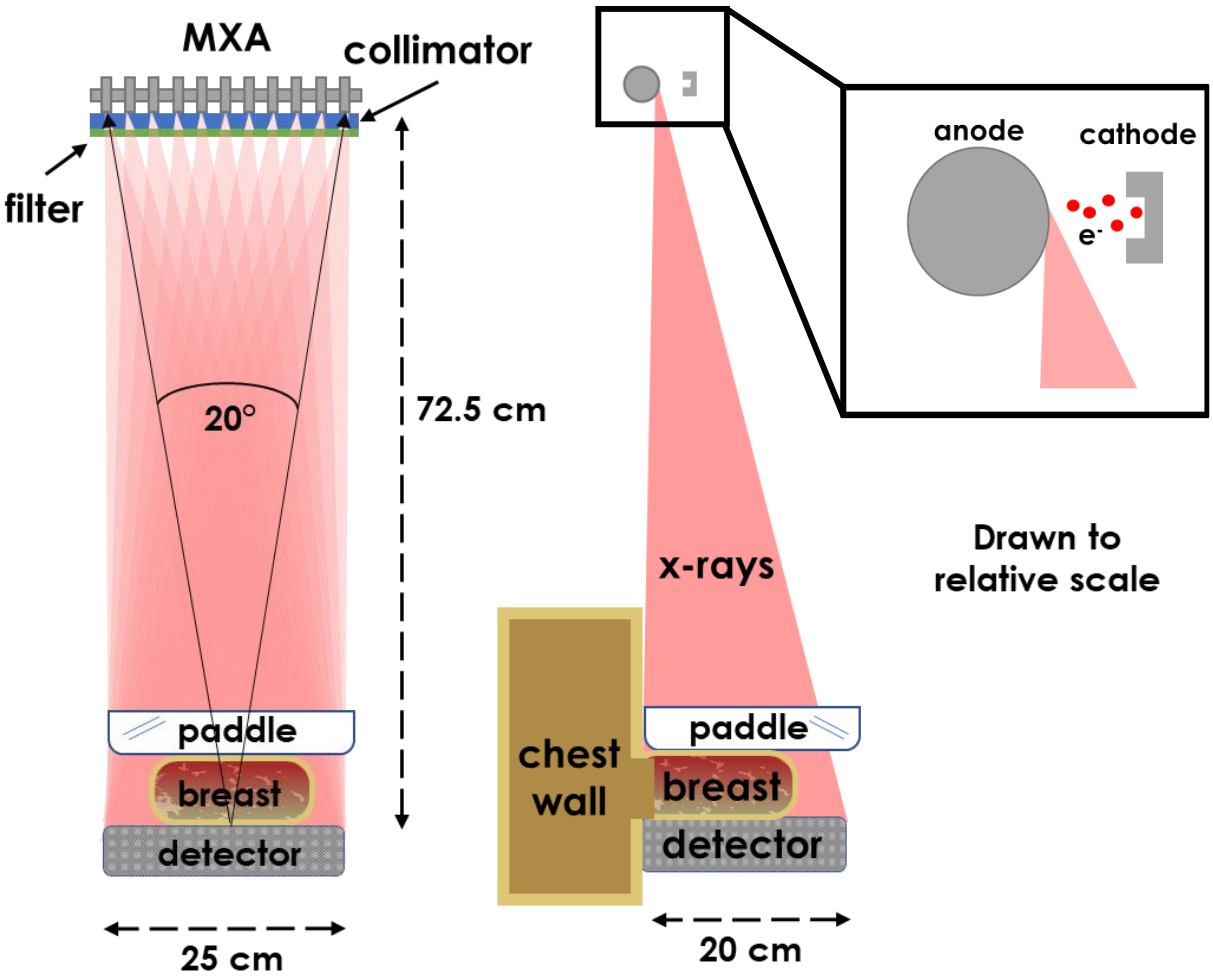

Figure 2.2. Schematic of the multi-source x-ray array (MXA) for digital breast tomosynthesis with the breast tissue positioned in the field of view.

Tomo Option). These are manageable powers and power densities given typical x-ray source duty cycles.

For prototyping studies two 3-source element and one 11-source element MXA sources were designed, built, and tested. The 3-element sources served as a prototype for the 11-element DBT source. Figure 2.3 is a photograph of the first 3-element prototype and shows the molybdenum rotating anode opposing three focus-cup grid-controlled tungsten filament cathodes. In this version the rotating anode was machined from molybdenum rod-stock. Prototyping for a DBT MXA source will allow comparison with a commercially available system. The 11-element anode was fabricated with a source separation of 2.3 cm (equivalent to a total scan angle of 20^{o}) to produce a projection number and scan angle between that of the Hologic Dimensions 3D (15 projections over 15^{o}) and the GE Senoclair system (9 projections over 25^{o}).

Although the machined-anode approach is physically robust and simple, it becomes costly and more difficult to fabricate as the diameter of the anode is increased for greater power handling

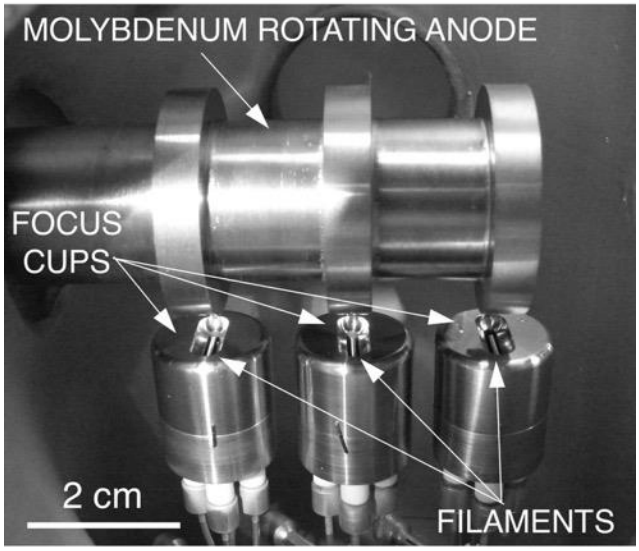

Figure 2.3. Photograph of the 3-source element MXA showing the solid molybdenum rotating anode and grid-controlled tungsten filament cathodes.

capability and/or the number of source elements is increased. This is because the amount of metal that is removed by the lathe is excessive with this approach. We have therefore transitioned to a modular approach in which anode components are fabricated and then brazed together.

The anodes were mounted on Varian RAD-92 x-ray tube rotor assemblies and driven by the associated Varian stator. For the 3-element prototype, a single RAD-92 bearing assembly was

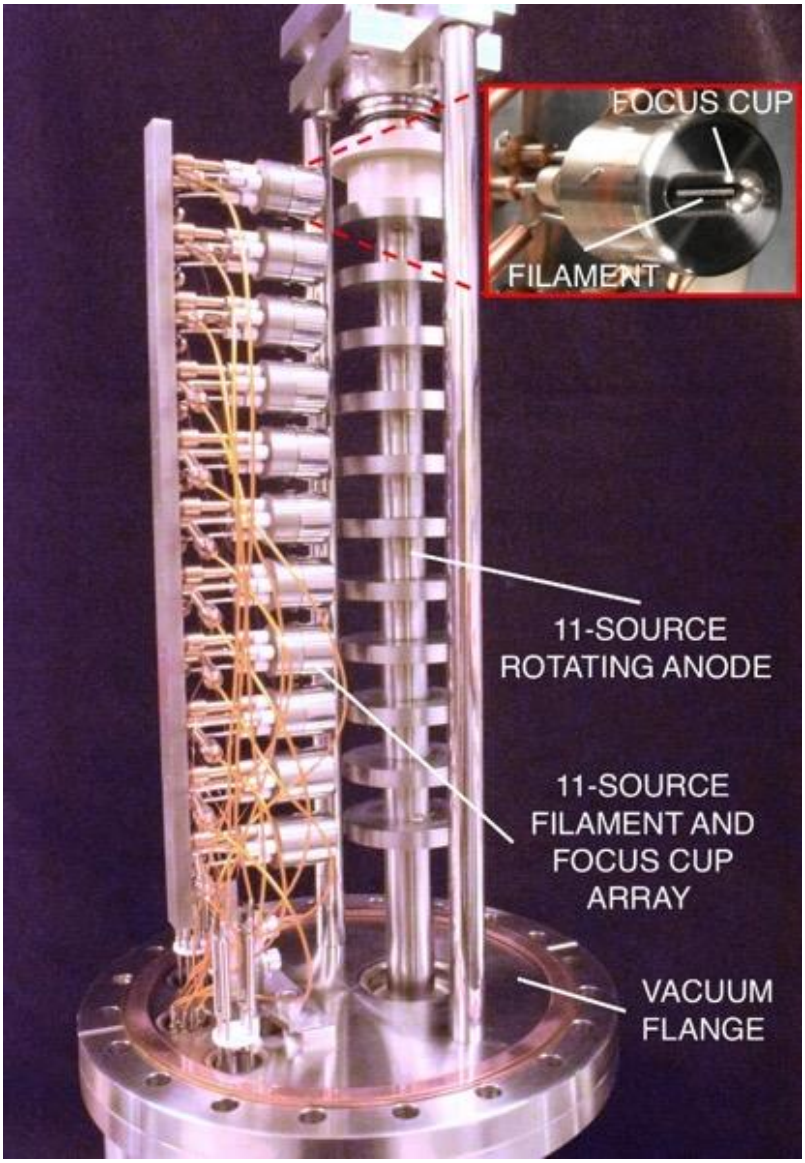

Figure 2.4. Photograph of the 11-source element DBT MXA with a close-up of the filament and focus-cup-grid assembly of one source element.

used. For the 11-source element MXA, two bearing assemblies were used with one at each end of the anode. Anode rotational speeds have been as high as 3600 rpm. The anode speeds were maintained at 1000 rpm to limit bearing wear and because the combination of current (limited to 50 mA at 45 kV by the generator, a Spellman STR120P6 high voltage supply) and focal spot size (0.3 mm x 1.0 mm) allowed these lower speeds. A photograph of the 11-source element MXA mounted on a demountable vacuum flange is shown in Figure 2.4.

The source elements are focus-cup grid-controlled with a focus cup (grid) bias of one to several hundred volts negative with respect to the grounded filament used to form the line focus on the anode. A grid bias of between -1000 V and -1200 V is used to turn off the x-ray source elements. The source elements are operated using an in-house, custom-built source controller which controls the beam current on the anode, the beam focusing and turn-off voltages of the grid, the exposure time of each source, and the time between turning on and off each source element. The filament current of each individual source element is controlled allowing for the resulting tube current from the individual elements to be adjusted/tuned, e.g. to be the same. In these prototyping experiments positive HV was applied to the anode to allow the filament and grid control circuity to be at ground potential.

Source studies were conducted using an ion-pumped stainless-steel vacuum envelope to house the MXA source (Figure 2.5). This chamber was operated in the 10^{-7} to 10^{-6} Torr range during experiments. The high voltage was applied to the RAD-92 rotor/stator assembly. Electrical feedthroughs supply the filament power and focus-cup voltages. A custom built, 1-mm-thick rectangular aluminum x-ray window with dimensions of 35 cm x 3.8 cm forms a vacuum seal at the bottom of the envelope. The current field of view at a source to imager distance (SID) of 65 cm is 21 cm x 30 cm, sufficient to accommodate our upgrade to a Varian 2520 detector in the future. No fundamental source constraints prevent having a field of view of 24 cm by 29 cm to be compatible with standard mammography/DBT detectors. Two commercial Conflat glass viewports were used to view the source assembly with a video camera during operation. No collimation was used for our prototyping experiments because the source was operated in an unoccupied room. Ultimately the MXA the collimator would nominally consist of a metal (such as lead or tungsten) plate having perforations that appear as parallelograms when viewed in cross-section from the

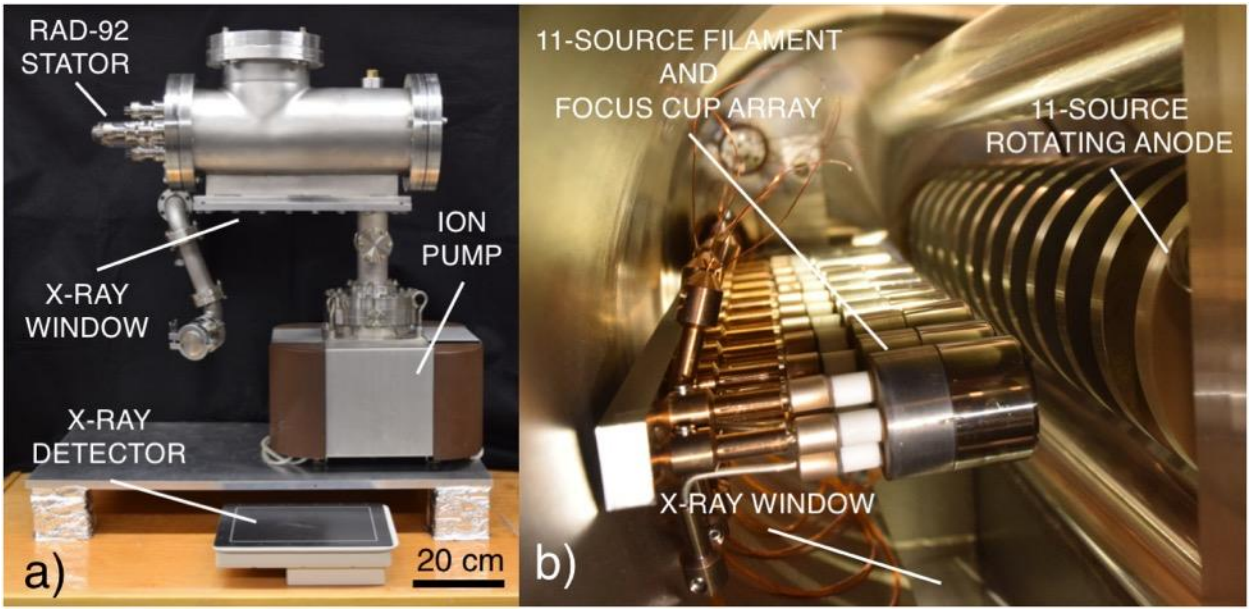

Figure 2.5. Photographs of a) The prototype DBT system used for the 3-source element and 11-source element MXA, and b) The 11-source element MXA installed in prototype DBT system.

edge of the plate. The orientation of the perforations can be designed to keep the x-ray coverage slightly smaller than the active area of the detector and constant for each projection to help minimize the risk of irradiating non-breast portions of the patient. This can be done in a relatively straightforward manner using, for example, water jet machining.

2.2.2. Anode angle and line focus

The anode target in this design does not have a traditional anode angle, however the effective anode angle is defined by the position of the cathode relative to the curvature of the perpendicular anode edge. The line focus geometry was implemented with the elongated portion positioned in the direction of anode rotation which is unconventional when compared to the standard anode design where the long axis of the focal track is normal to the direction of anode rotation. Generally, the heel effect is a result of anode self filtration that causes falloff in the intensity toward the anode. The unconventional design of this tube will result in a heel effect that occurs across the medial-lateral direction rather than the posterior-anterior direction.

Utilizing this unconventional design for a given anode rotational speed and incident electron beam power density, this decreases the power loading by a factor of 4. (The filament has a length of 5 mm which is roughly the beam spot length on the anode, and the width of the beam on the anode was measured to be 0.3 mm, therefore $[5\ \text{mm}/\ 0.3\ \text{mm}]^{1/2} \sim 4$). This design was more straightforward geometry to employ for our prototyping studies. Estimates indicate that a 5 cm diameter anode at 1000 rpm and an anode angle of 12° with 11 source elements can accommodate exposures of 100 mAs at 40 kV with 100 mA/(source element). The geometry was set to an effective anode angle of 12° for all the experiments reported here.

The existing geometry allows for the anode angle to be varied *in situ* by deflecting the electron beam from each source element in the direction perpendicular to the rotational axis of the anode. This deflection could be implemented using a second grid electrode placed between the focusing cup and the anode. In the existing assembly, the anode angle could be varied from a few degrees to several tens of degrees. Changing the anode angle has a significant influence on the effective size of the focal spot, the x-ray fluence rate, the heel effect, and the field coverage of the beam at the detector.

2.2.3. Source evaluation

Fundamental operating parameters of the MXA source investigated were the x-ray spectrum, x-ray focal spot size, tube output, half value layer (HVL), and source modulation characteristics. The x-ray spectra were measured using an Amptek XR-100 detector calibrated with ^{55}Fe and ^{241}Am x-ray standards.

The focal spot size measurement can be performed in several ways, and in this study both a pinhole camera and a star pattern are utilized for two distinct measurements. A pinhole camera uses a thin, highly attenuating material with a small circular aperture positioned on the central axis and the focal spot is measured as the spread of the pinhole response at the detector. A star pattern test tool has a radial pattern of spokes with diminishing width and spacing, and the "equivalent" focal spot size is measured as the distance between the outermost unresolved spokes. These tools are illustrated in the schematic diagram in Figure 2.6.

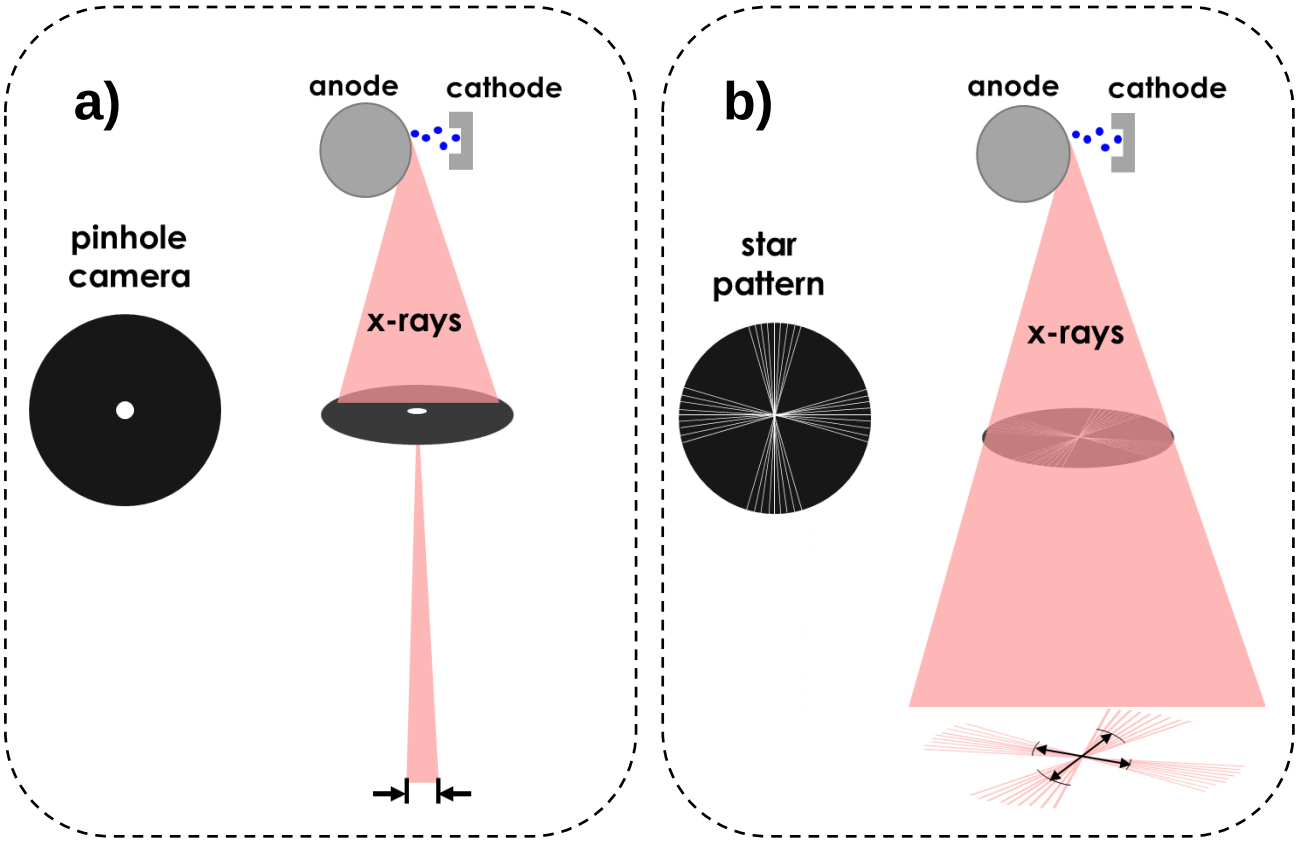

Figure 2.6. Schematic diagrams showing two tools for measuring the focal spot size from an x-ray tube (a) with a pinhole aperture and (b) with a star pattern.

In this study, the focal spot size was measured directly using a 10 μm diameter pinhole (Nuclear Associates, Inc., Carle Average) and the "equivalent" focal spot size was measured using a star x-ray test pattern (Model 07-503, Nuclear Associates, Inc., Carle Place, NY, USA) which contains 60 spoke pairs divided into four 15° sectors wherein each spoke diverges at an angle of 0.5°). Equation 1.1 was used to calculate the effective focal spot size (f) with the star pattern, where θ is the angle of the spokes, M is the known magnification, and d is the blurred diameter of the star pattern image at the detector.

$$f = \frac{\pi\,\theta}{180}\,\frac{Md}{M-1} \tag{1.1}$$

The tube output and HVL measurements were made using a dedicated mammography ionization chamber (10X5-6M-3, RadCal Corp., Monrovia, CA, USA) connected to a model 9060 electrometer and a model 9010 readout unit (RadCal Corp., Monrovia, CA, USA). The measurements of the x-ray pulse shape versus time were taken using an Amperex XP2262B photomultiplier tube and plastic scintillator with the output viewed by a Tektronix TDS540D oscilloscope.

Initial imaging characteristics of the prototype source were evaluated using a Varian PAXSCAN 1313 flat-panel x-ray detector based on an indirect thin-film transistor design and a CsI scintillator. The 1313 panel incorporates 127 μm pixels over a 13 cm x 13 cm field of view. The array of 1024 x 1024 pixels can be read out at up to 30 frames per second. The electronics associated with the flat-panel detector provides a 5 V transistor-to-transistor logic (TTL) pulse for each frame and this TTL pulse was integrated with the source controller to synchronize the firing of each x-ray source element. The source-to-detector distance was 72.5 cm. We have since transitioned to the use of a Varian 2520 detector, which simply replaces the position of the Varian 1313 detector.

Tomographic data sets and x-ray modulation experiments reported here were made with the 3-element MXA source serving as a prototype for the 11-element source. This is because the 11-source element controller, for which the 3-source element controller served as a prototype, is still under construction. In order to mimic the tomographic data set produced by an 11-element source, the detector was physically translated under the MXA source (3 element source position 1 served as 11-element source positions 1, 4, 7 and 10; 3 element source position 2 served as 11-element source positions 2, 5, 8 and 11; 3 element source position 3 served as 11-element source positions 3, 6 and 9. A phantom used for geometrical calibration was made by cementing 1/16”

(1.59 mm) diameter stainless-steel spheres onto a 1/32”-thick (7.9 mm) sheet of polymethylmethacrylate sheet (i.e. Lucite™), to form a regular right pyramid, with one sphere at the apex and one at each of the four corners of the base. The base side-length of the pyramid was 1 cm and the height of the center of the sphere at the apex above the center of the spheres at the base was 8 mm.

2.3. Results

2.3.1. X-ray spectra

Figure 2.7 shows the x-ray spectrum from a single source element using electron beam energies ranging from 25 to 45 keV (in 5 keV intervals). The higher energies are typical for those required in DBT. The *K*-shell fluorescence lines of molybdenum at 19.6 keV and 17.4-17.5 keV are evident as peaks in the spectrum and the highest peak was used to normalize the counts in the spectrum. No discernable difference was observed between the spectra produced by the 11-source elements as expected using the same electron energy and x-ray beam filtration with each element. The kV was set to provide energy given and the mA was adjusted to prevent pulse ‘pile-up’ in the detector,

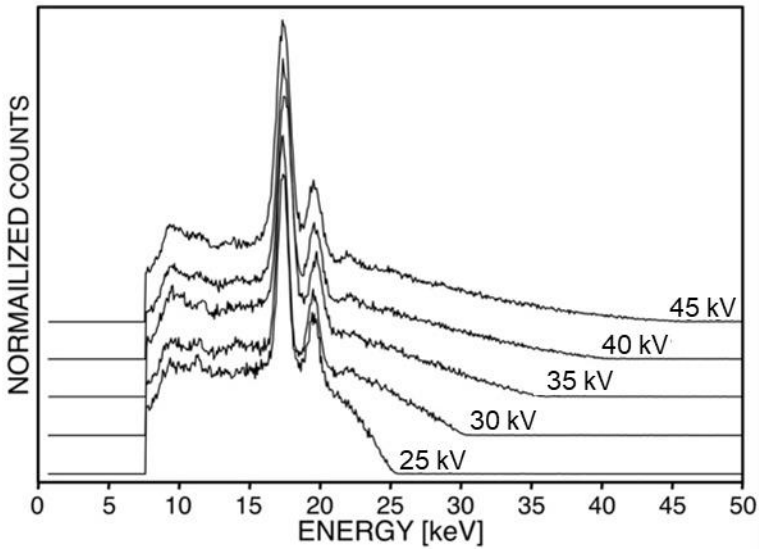

FIG 2.7. X-ray spectrum of a typical source element operating at an electron energy range from 25 keV to 45 keV in 5 keV increments.

which results in the spectrum drop off at the maximum energy for each curve. The offset in the spectra was added for the purpose of visual discrimination between the curves and does not correspond to real shifts in the data.

2.3.2. X-ray focal spots

Figure 2.8 shows x-ray pinhole camera images of a typical x-ray focal spot from a single source element as a function of voltage, V_{grid} , applied to the focus cup grid relative to the grounded filament. As V_{grid} is decreased from 0 V there is a gradual decrease in the size of the focal spot perpendicular to its elongated direction. Optimal focusing was achieved with a V_{grid} between -200 V and -300 V for anode voltages between 35 kV and 45 kV. Here, about 80% of the x-rays emanate from within 0.3 mm of the spot centerline. As V_{grid} is decreased further, the spot becomes over focused and begins to broaden while there is a slight decrease in the width of the focal spot in the elongated direction as is evident in Figure 2.8 at - 400 V. A V_{grid} of -1200 V reduced the anode current to zero amperes. The pinhole images were taken with the pinhole located slightly on the filament-side of the vertical line connecting the x-ray focal spot with the detector surface to view the focal spot without excessive geometrical foreshortening by the line focus principle.

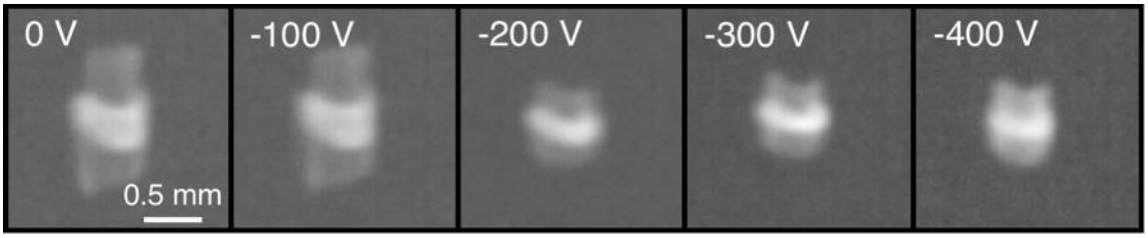

FIG 2.8. X-ray pinhole camera images of the x-ray focal spot as the grid bias (focus cup bias) is changed. 45 kV, 50 mA.

An x-ray star pattern radiograph (Fig 2.9) was taken with the same source element used to produce the pin-hole camera images. The star pattern was centered in the x-ray beam striking the detector, and the effective focal spot size was determined to be 0.30 mm. In this position, the focal spot appeared to have nearly equal dimensions from each of the 11-source elements and varied by less than ~ +/- 10%.

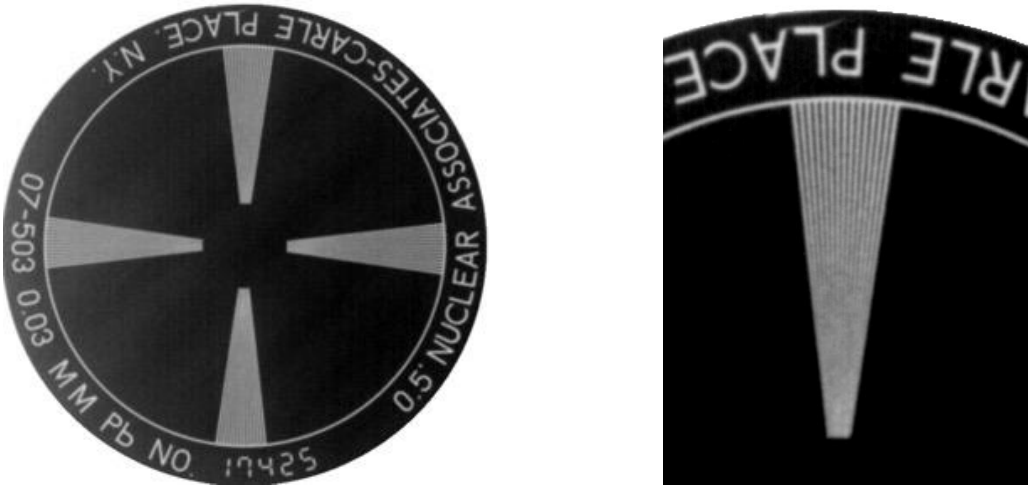

FIG 2.9. X-ray star pattern of a typical individual source element. Spot size is 0.3 mm x 0.3 mm for V_{grid} = -300 V at 45 kV and 50 mA. Magnification on detector = 1.8X.

2.3.3. X-ray tube output

Figure 2.10 shows the tube output measured as a function of beam energy from 20 kV to 45 kV (in 5 kV intervals) for a single source element (Fig 2.9). The filament current of each source element can be independently controlled and the output of each energy level at each source is reported in Table 2.1 with the mean and standard deviation across source elements.

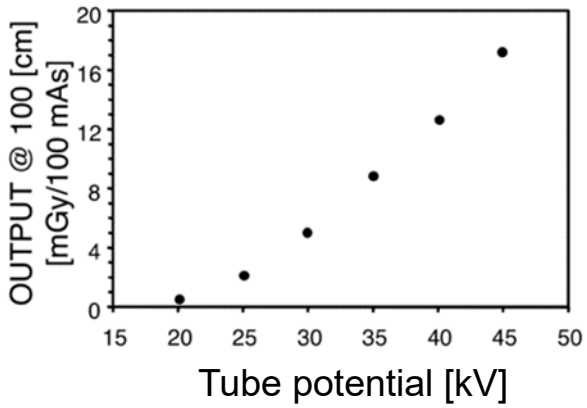

FIG 2.10. Tube output from a typical element of the 11-source element MXA as a function of tube potential.

Table 2.1. Tube output [mGy/100 mAs @ 100 cm] for 11 sources reported as individual measurements from 11 sources with the mean and standard deviation across the 11 sources.

[kV]	S1	S2	S3	S4	S5	S6	S7	S8	S9	S10	S11	MEAN	SD
20	0.50	0.50	0.60	0.50	0.60	0.60	0.50	0.60	0.60	0.50	0.60	0.55	0.05
25	2.10	2.20	2.30	2.10	2.10	2.20	2.20	2.30	2.10	2.20	2.20	2.18	0.07
30	4.90	4.90	5.20	5.10	5.00	5.10	4.90	5.10	5.00	5.10	5.20	5.05	0.11
35	8.70	8.70	9.10	9.00	9.20	8.90	8.70	8.70	9.00	8.60	9.10	8.88	0.20
40	12.50	12.80	12.50	12.60	13.00	12.70	12.70	12.60	13.00	12.60	12.70	12.70	0.17
45	17.00	17.60	16.90	17.20	17.60	17.30	17.70	17.30	17.40	17.70	17.00	17.34	0.28

2.3.4. Half-Value Layer

The HVL was measured at 50 mA at beam energies of 30 kV, 35 kV, 40 kV, 45 kV using the molybdenum anode with the 1-mm of aluminum filtration built into the tube housing (Fig 2.11).

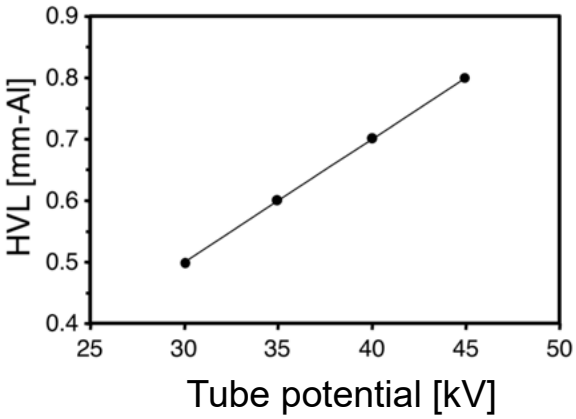

FIG 2.11 Half-value layer measured with the 11-source element MXA at 50 mA.

2.3.5. X-ray modulation

The focus-cup grid control was designed to be compatible with DBT systems using from 9 to 25 projections because these represent the range of most existing major manufacturer's systems.[15] A nominal total exposure for DBT of 100 mAs can be achieved with an operating current of 100 mA/source element, and an appropriate DBT detector (such as the Varex Dexela CMOS 2923, which has 0.075-mm native detector elements and operates at 26 fps in the 1 x 1 binning mode), With these assumptions the maximum on-time for a given source element is (100 mAs / [100 mA/source] / 9 sources) = 111 ms, at a source element switching frequency of (111 ms + 1/26 fps) = 149 ms/projection equivalent to ~ 7 Hz. The minimum on-time per source element and maximum operating frequency would occur with the source elements operating at the estimated[12] 200 mA maximum of our system with 25 projections. In this case the individual source element on-time is

(100 mAs / [200 mA / source] / 25 sources) = 20 ms giving a source switching time of (20 ms + 1/26 fps) = 59 ms/projection equivalent to a rate of 17 Hz.

Figures 2.12 and 2.13 show sequential x-ray pulses for each of the three individual elements comprising the 3-element MXA in the low and high-speed switching cases above using currents of 40 mA at 35 kV. Figure 2.12a shows the TTL logic pulse used to control the focus cup grid potential and switch it from -1200 V (x-ray off) to -200 V (x-ray on at minimum focal spot). When the TTL signal is high the source is on and when the signal is low the source is off. Figure 13b shows the X-ray output versus time with 110 ms wide x-ray pulses sequentially from each of the three MXA source elements at 7 Hz. Similarly Figure 2.12b shows the x-ray output versus time with 20 ms wide X-ray pulses sequentially from each of the three elements at 17 Hz. Together Figure 2.12 and Figure 2.13 show that the times required to modulate the x-ray output from each source element can address any of the range of possibilities required for existing DBT system designs. Note that because the output of each source element can be adjusted independently of the others by setting different filament currents, small variations in x-ray output between source elements can be achieved.

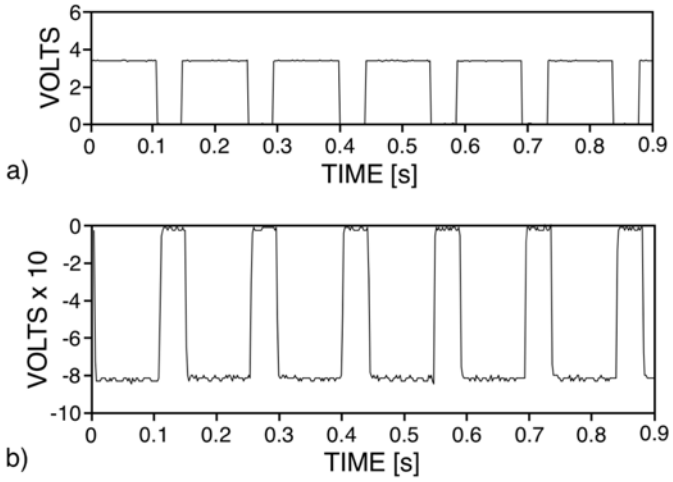

FIG 2.12. Oscilloscope traces of the 3-element source cycling through each source element in sequence. a) The TTL logic pulse used to control the grid voltage. TTL high turns on the source; b) The signal from the x-ray detector showing a 110 ms duration x-ray pulse at a frequency of 7 Hz. The ON signal is at -0.8V and the OFF signal is at 0V.

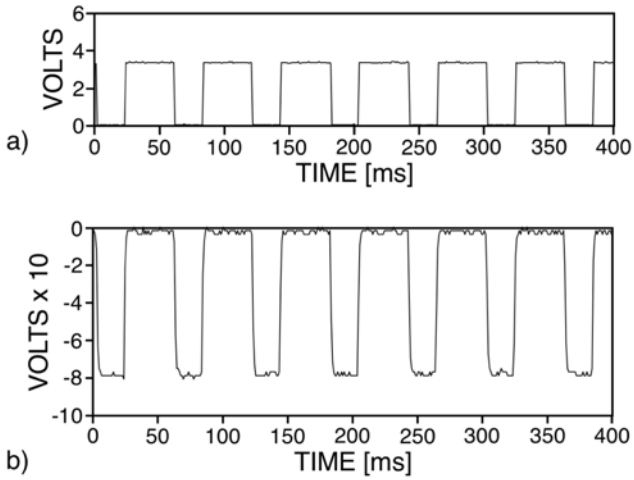

FIG 2.13. Oscilloscope voltage versus time plots of the 3-element source cycling through each source element in sequence: a) The TTL logic pulse used to control the focus cup grid voltage; b) The signal from the x-ray detector showing a 20 ms duration x-ray pulse at a frequency of 17 Hz. The ON signal is at -0.8V and the OFF signal is at 0V .

2.3.6. Tomosynthesis data

Figures 2.14 and 2.15 are examples of tomosynthesis images reconstructed from data taken using the MXA. The orientation of the images is such that the right-hand side of the image is the anode-side of the MXA source. The total exposure was 100 mAs (9.1 mAs/element operating at 45 kV and 50 mA/element) in both cases. Figure 2.14 shows tomosynthesis images of the BB-calibration phantom at three depths with the planes separated by 4.0 mm. Fig. 2.14a shows the plane in which the BB at the apex of the pyramidal phantom is in focus; Fig. 2.14b, the plane half-way between the BB at the apex and the four BBs at the base of the pyramid; and Fig. 2.14c the plane in which the four BBs at the base of the pyramid are in focus. Figure 2.15 shows tomosynthesis images of an orange at three depths with the planes separated by 4.0 mm through the central core. The projections were reconstructed using simple shift and add for the BBs and matrix-inversion tomosynthesis for the orange. These are the first reconstructions of tomographic data sets for the MXA source and in the future higher contrast objects will be scanned.

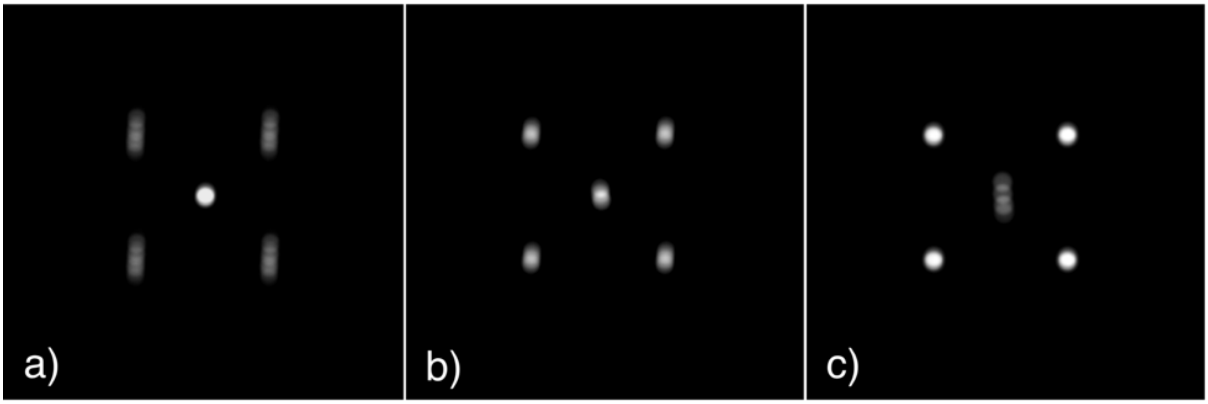

FIG 2.14. Tomosynthesis images of the BB-phantom at three depths showing planes separated by 4.0 mm. The single BB at the apex of the right regular pyramid is furthest from the detector

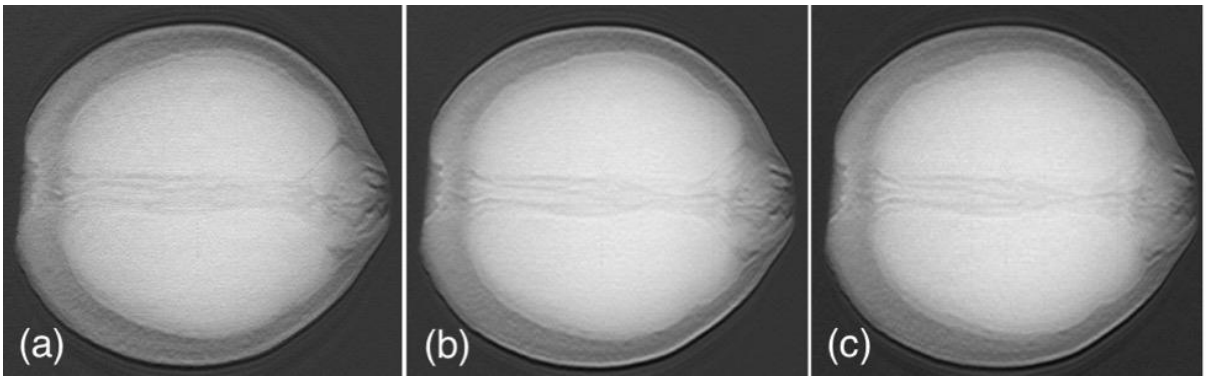

FIG 2.15 Tomosynthesis images of an orange at three depths showing planes separated by 4.0 mm through the central core centered on the plane shown in (b).

2.4. Discussion

2.4.1. X-ray spectra

The standard bremsstrahlung spectra from a molybdenum anode was shown in Figure 2.7. Monte Carlo simulations and analytical modelling[32] have indicated that roughly 1-mm of aluminum, as used in these studies, provides good filtration for DBT when tungsten anodes are used. However, the spectra results with the aluminum tube port filter included low energy spectrum components that are not necessary for breast cancer imaging. When using a molybdenum anode, it may be more beneficial to apply a molybdenum or rhodium filter to remove the low dose components of the spectrum. Longer term plans for this technology include cladding the molybdenum focal tracks with a tungsten/rhenium alloy, because tungsten offers a much higher melting point and greater bremsstrahlung production than materials of lower atomic number. Both molybdenum and rhodium provide useful characteristic x-rays for breast imaging. Tungsten anodes are being used more frequently for breast imaging, with appropriate beam-softening filters such as rhodium, palladium, and silver. This cladding technique is commonly employed outside of breast imaging applications for general purpose radiography and computed tomography.

2.4.2. X-ray focal spots

Focal spot behavior with focus cup voltage is consistent between different source elements and spot sizes are consistent with those used in DBT. Note that the spot intensity distribution is not bimodal and this result is to be expected when using biased (as opposed to nonbiased) focus cups.[33] There are a number of geometrical variables that impact the focusing voltage required to optimize the spot size and turn-off the source element including the position of the filament within the focal cup, the dimension and shape of the cup, and the proximity and potential applied to the anode.

Electron optical modeling of the focus grid electrode using commercial software (COMSOL) with a particle tracing module was applied to investigate the trade-offs involved in control focusing of the beam onto the anode. The current design has not been optimized but improved by trial and error by varying the field on the filament, the anode-to-cathode distance, and the depth of filament in the focus cup.

2.4.3. X-ray tube output

The increasing x-ray production efficiency at higher voltages is evidenced by the increase in slope of the curve with increasing voltage (Figure 2.10). The output of the MXA is comparable to that of clinical DBT systems. The operating current of 50 mA/source yields an air kerma rate of 5 mGy/s at 28 kV with the typical SID for mammography/DBT of 65 cm. Typically the output is approximately proportional to the square of the tube voltage (exposure $\propto kV^2$) however this trend was not observed in this data, which could be a result of the anode and filter material combination (molybdenum and aluminum) applied in these experiments.

2.4.4. Half-Value Layer

The beam quality reported here meets the requirements set by the MQSA and the ACR for the range of half-value layers that are applicable for mammography with a *Mo* target and *Rh* filter combination. The effective x-ray energies referenced to the measured half-value layers are roughly, 18 keV (0.5 mm *Al*), 19 keV (0.6 mm *Al*), 20 keV (0.7 mm *Al*), and 21 keV (0.8 mm *Al*).

2.4.5. X-ray modulation

Key to the operation of the MXA source is modulation of the x-ray output from each individual source element with the focus cup grid voltage, referred to as *grid control*. The modulation rate is linked to the scan time, i.e., the time required to generate the entire tomographic data set. As would

be expected, x-ray element modulation times using grid-control techniques can be in the millisecond range and source on-time and modulation rates demonstrated here are easily high enough to handle current levels of 200 mA/source element. Scan time is in part dictated by the x-ray tube current and the application. The Hologic DBT system has the shortest scan time of commercial systems at 3.7 s for 15 projections (~70 mAs exposure). Field electron emission-based stationary sources using stationary anodes have a scan time of ~ 3.1 s.[8] Currently, the MXA even operating at the demonstrated 50 mA/source element, has a scan time for 15 projections at a 70 mAs exposure of (15 projections/26 fps + 70 mAs/50 mA) = 2.0 s, where we have assumed use of an appropriate DBT detector such as the Varex Dexela CMOS 2923 which has 0.075-mm native detector elements and operates at 26 fps in the 1x1 binning mode. The potential of the MXA to further reduce scan time is significant. The MXA scan time would be 1.3 seconds when operating at 100 mA/source element. The scan time would be reduced to 0.9 s when operating at 200 mA/source element and then the detector frame rate will become the limiting factor with respect to total acquisition time. A summary of clinically available systems is reported in Table 2.2 with the scan angle, number of projections, scan time, and then the proposed scan time and required frame rate with an MXA integrated into a comparable DBT system.

Table 2.2 Summary of clinical DBT systems scan parameters and the proposed scan times with MXA integration operation at 50 mA, 100 mA, and 200 mA.

Parameter	Hologic Selena Dimensions	GE SenoClaire GE Senographe	Siemens Mammomat	Fujifilm Aspire
Scan angle (deg)	15	25	50	14 - 40
Number of projections	15	9	25	15
DBT scan time (sec)	3.7	10/7	25	7-9
MXA-DBT scan time @ 50 mA/source element	2.0 s @ 7 fps	2.0 s @ 5 fps	2.0 s @ 13 fps	2.0 s @ 7 fps
@100 mA/source element	1.0 s @ 15 fps	1.0 s @ 9 fps	1.0 s @ 25 fps	1.0 s @15 fps
@200 mA/source element	0.5 s @ 30 fps	0.5 s @ 18 fps	0.5 s @ 50 fps	0.5 s @ 30 fps

2.4.6. Tomosynthesis data

The first studies of reconstructing tomographic data sets from the MXA source used matrix inversion tomosynthesis (MITS). Previous studies have shown that MITS[34] can be more accurate than simple filtered backprojection (FBP). In the future, FBP will be applied with the standard ramp filter and the cosine-shaped apodization filter to suppress high-frequency noise. The low frequency enhancement[34,35] will be used to restore some of the contrast suppressed by the ramp filter, which will also reduce the "flat" appearance. With MITS, the sliding average approach that sums adjacent planes[36] will be optimized for the number of slices to slab according to the response of microcalcifications with the given tube angle used. This sliding average technique reduces image noise while also suppressing most tomosynthesis artifacts. For FBP, a slabbing method will be used to best depict the three-dimensional spread of microcalcification clusters.

2.4.7. Source-element performance consistency

Even though the MXA is only in the initial prototyping stage it is worthwhile to discuss aspects related to the consistency of performance between source elements. To date reasonable consistency between source elements in terms of spectral output, x-ray focal spot size, x-ray output, and tube (anode) current has been reported. One aspect of the MXA that allows for matching the performance between individual source elements is that the filament current through each element can be controlled independently. This means that the tube current due to each source element can be adjusted to balance the x-ray output and achieve highly similar outputs as shown in Figures 2.12 and 2.13. We note that this control of the output allows one to vary the output of each source element to keep the x-ray fluence rate at the detector constant. This is important to adjust as the detector-to source element distance changes, which is true in the case of the prototype's linear array geometry. The x-ray focal spot sizes can be made very similar to one another across the array of 11-source elements, mainly by adequate control of geometrical variables just as is done for conventional commercial tubes of the same model. In addition, the grid-control feature of the MXA allows for the use of different focus voltages for each source element to adjust to the focal spot size.

Long-term source stability studies are a future task because this is the prototyping stage. However, we have qualitatively observed over the course of hundreds of experiments that involved cycling through source elements over weeks of operation that filament current-voltage characteristics and the resulting tube currents are reproducible, and x-ray output per source element is consistent. The MXA design is the result of the integration of proven tube components to make an array of conventional tungsten-filament-based, grid controlled, rotating-anode x-ray sources operating in parallel within a common vacuum envelope. From this top-level view, one would then

expect that the key characteristics such as the inherent lifetimes and stability associated with filament performance, the reproducibility of source element output, and spot size variations between elements to be similar to that achieved with and between conventional rotating anode x-ray tubes of the same model, e.g., according to IEC standards.

2.4.8. Anode considerations

Molybdenum anodes were used because molybdenum can be machined into various shapes by conventional methods, and because the power loading capability of molybdenum was adequate for initial testing. The x-ray tube current was limited to 50 mA by the x-ray generator. A transition to tungsten/rhenium cladding on the focal tracks on the anode is planned because it would not only provide an x-ray energy distribution that is better matched to DBT and CT imaging applications, but also would increase the allowable x-ray flux and power loading (W/cm2) levels compared to molybdenum due to its higher *Z* and higher melting point.

The geometry of the MXA anode allows for effective cooling for a few reasons. First, the large surface-area-to-volume ratio of the MXA anode disk array increases its efficiency in radiating power relative to a standard rotating anode. The MXA anode shown in Figure 2.3 has roughly twice the effective radiating surface area as a conventional 4” diameter rotating anode and the radiated power is proportional to the radiating area. Secondly, liquid-cooling of the anode can be implemented by flowing the liquid (e.g., water) along the axis of the anode, i.e., in one end and out the other, possibly employing ferrofluid seals for the vacuum-to-atmosphere anode seal and water supply-to-anode seal. Roughly speaking it is practical to dissipate over 10 kW with water flow through a hollow-cylinder-based version of the anode shown in Figure 2.3, whereas typical

values of power dissipation by conduction through the ball bearings of a conventional tube are of order a few watts.

The modular approach to fabricating the anode enables the design of more advanced anode configurations, such as stacked disks having diameters that gradually increase from the center of the field of view outward - with the anode faces machined at a fixed angle relative to the axis of rotation. This would mechanically steer the focal spot toward a common isocenter and result in all the focal spots located on a radius of curvature centered on the isocenter of the tomosynthesis system. Such a design would keep a constant x-ray focal spot size and source-to-isocenter distance by emulating the path of a single x-ray tube traveling through an arc. In addition, this design would only need a simple, cylindrically symmetric vacuum envelope enclosure around the MXA source assembly. This would require that the focal spots be spatially located on a compound curve, and this fabrication strategy is straightforward. A curved source array would allow use of existing tomosynthesis reconstruction algorithms and balancing focal spot shape and size across all sources would reduce potential image artifacts.

2.4.9. Line focus and in situ variable anode angle

The ability to change the effective focal spot size over a wide continuous range of dimensions has several usable applications in breast imaging and beyond. Decreasing the anode angle results in both a smaller x-ray focal spot and a smaller usable field of view. For magnification mammography and tomosynthesis applications, the anode angle could be dynamically adjusted to accommodate the variable field of view used in magnification imaging, allowing the smallest effective focal spot to be used for each field-of-view setting. Given the speed of acquisition capable with the MXA, each source element could produce two redundant images for each tomographic projection – one with a large focal spot and one with a smaller focal spot. This would result in one acquisition being

high-pass and the other medium-pass filtered. With the appropriate use of image processing software (such as subtraction or deep learning versions of subtraction), harmonized (*e.g.*, blurred-mask subtraction) projection images could be used to produce edge-enhanced (using physics, not just image processing) tomosynthesis reconstruction.

2.5. Conclusions

The proof-of-principle experiments were performed and demonstrate the feasibility of the MXA source technology, comprised of an array of grid-controlled tungsten filaments and a rotating anode. The first prototype demonstrated operating characteristics consistent with x-ray tubes required for stationary source DBT. The functional MXA system was demonstrated, and tomosynthesis images were produced – demonstrating the first application of a tomosynthesis system employing a stationary x-ray source comprised of thermionic cathodes and a monolithic rotating anode. The MXA had shown the potential to significantly reduce scan times relative to existing and proposed commercial systems.

Future goals are to increase the rotational speed of the anode to 3600 rpm or beyond and extend the tube current to 200 mA per source. Plans are in place to purchase a new generator providing 200 mA at 50 kV. A larger field-of-view flat panel detector (Varian 2520 with 0.127 mm detector element dimensions [Salt Lake City, UT]) is currently being integrated into a compact tomosynthesis system for further imaging experiments.

Chapter 3: Cone beam CT multisource configurations: evaluating image quality, scatter, and dose using phantom imaging and Monte Carlo simulations

3.1. Introduction

There are known general disadvantages of CBCT that need to be better investigated to ensure that image quality and clinical outcomes are not compromised when switching from MDCT to CBCT. First, the common circular trajectory of the source is a known limitation because it does not meet the Kirillov–Tuy condition[37] for complete 3D image reconstruction – leading to inherent cone beam artifacts along the z-axis and incomplete sampling in the Fourier domain. These artifacts are most pronounced at large cone angles resulting in inconsistent image quality[38] throughout the field of view (FOV) which can reduce the diagnostic quality and quantitative integrity of CBCT when compared to MDCT. A second limitation of CBCT is the size of the object that can be scanned, since the maximum object FOV is smaller in CBCT than MDCT. Another limitation for CBCT applications in image guided therapy is that the planning target volumes often require multiple scans to cover the entire area of interest, which extends the total scan time. CBCT also suffers more from scatter than MDCT, due to the larger x-ray beam field size, and this increases noise and decreases contrast resolution[39,40].

A common problem with traditional CBCT reported in clinical comparisons between MDCT vs. CBCT was the inconsistency in image quality throughout the FOV (i.e., better image quality near the central ray and worse toward the periphery of the field of view) generally caused by scatter, noise, and artifacts. Several groups have made direct comparisons between CBCT vs.

MDCT for clinically relevant tasks and these studies reveal the limitations of current CBCT for various[41-42] clinical applications.

For image guided radiotherapy, the limited FOV and inaccurate Hounsfield Unit (HU) values of CBCT were shown to cause inaccuracies in treatment planning when compared to MDCT in both phantom and patient cases.[41] For the characterization of musculoskeletal trauma in cadaver knees and hands, it was shown that MDCT was favorable to CBCT by radiologists for soft tissue tasks[43]. In a large cohort patient study[44] comparing MDCT to CBCT, post-traumatic finger fractures were missed in CBCT. Another study that compared the application of MDCT and CBCT in cadaver wrists found that CBCT was less sensitive than MDCT at detecting fractures[45]. CBCT applied to orthodontics in cadaver studies was shown to result in large and frequently inaccurate bone height measurements when compared to physical measurements[46] and was also shown to be less accurate than MDCT for bone density evaluation[42].

There have been efforts to overcome the under sampling problem in CBCT, with multisource x-ray source configurations,[47] computer simulations of inverse CBCT systems,[48,49] prototype development of inverse CT systems[50], and development of correction techniques in the image reconstruction algorithm[51,52]. Complex geometries (e.g. helical, saddle, line and circle) aim to meet the Kirillov–Tuy condition[37], but at the expense of complicated hardware and mechanical alignment systems. Multiple individual x-ray sources have been applied to CBCT and have shown improvements in the reduction of cone beam artifacts with a physical prototype[47], but still suffer from photon scatter caused by large field sizes. Numerical simulations have been used to study multiple parallel circular cone beam orbits,[53,54] the saddle geometry[55], the line and circle geometry[56], multithreaded cardiac CT[57], helical cone beam CT[58] semi-stationary CT[59] and stationary CT[60].Current methods for scatter correction in CBCT include physical collimators and

anti-scatter grids[61], as well as software correction algorithms based on Monte Carlo estimation[62,63], physical measurements[64,65,66] or postprocessing in the image domain[67].

This study will preserve the simplicity of the circular trajectory in CBCT with analytical image reconstruction while overcoming the limitations of cone beam artifacts and scatter caused by large field sizes, extending the FOV, and distributing the dose more effectively. This solution could offer improved image quality in the many applications that suffer from artifacts caused by the non-ideal geometry in conventional CBCT.

Physical experiments were performed to evaluate image quality using a prototype CBCT system and Monte Carlo simulations were applied to evaluate the 3D dose distribution in a voxelized polyethylene phantom and scatter contributions in the projection domain for various multisource configurations. Three multisource geometries were considered with two different collimation schemes. Traditional CBCT collimates the x-ray beam to cover the entire detector at once, and when applied for multisource techniques this will be referred to as the overlapping multisource geometry. We also consider a different approach to achieving full detector coverage in CBCT by stacking several small cone angle exposures, which will be referred to as the collimated multisource geometry. The field of view for the reconstructed image domain remains the same across the comparisons.

3.2. Methods

3.2.1. Source configuration concept

Diagrams in Figure 3.1 show the x-ray source positions and corresponding FOV sizes for the different source configurations considered in this study. Three multisource geometries were considered with two different collimation schemes. The CBCT collimation scheme that covers the

entire detector at once will be referred to as the *overlapping* multisource geometry (Figure 3.1b and 1c). We also consider a different collimation scheme by stacking several contiguous small cone angle acquisitions, which will be referred to as the *collimated* multisource geometry (Figure 3.1d). In this study, six source locations with 30 mm separation between each source were simulated in both the overlapping and collimated geometry. Each vertical source position is assigned a letter (A-F) and those positions were constant across all geometries and experiments. Comparisons were made between the four different CBCT source configurations: (i) a one source, (ii) overlapping three source, (iii) overlapping six source, and (iv) collimated six source.

The ideal collimation system is depicted in Figure 3.1, where the sources are uniquely collimated to cover the FOV with adjusted posterior and anterior cone angles. For the three-source overlapping configuration (Figure 3.1b) the cone angle of position A is 2° posteriorly and 14° anteriorly, for position C the cone angles are 6.9° posteriorly and 9.3° anteriorly, and for position E the cone angles are 11.7° posteriorly and 4.5° anteriorly. Similarly, for the six-source overlapping geometry the cone angles of position A are 2°/14° (anterior/posterior), position B cone angles are 4.5°/11.7°, position C are 6.9°/9.3°, position D are 9.3°/6.9°, position E are 11.7°/4.5°, and position F are 14°/2°. This ideal collimation scheme was applied in the Monte Carlo simulations explained in section 3.2.8 However, the physical experiments (detailed in section 3.2.2) utilize a rigid collimation system (i.e., 2° posteriorly and 14° anteriorly) which cannot be adjusted and was predetermined by the built-in x-ray tube housing. For the collimated system geometry, additional collimation was added anteriorly resulting in a 2° cone angle both anteriorly and posteriorly (Figure 3.1d) and consistent for both the physical experiments and the Monte Carlo simulations.

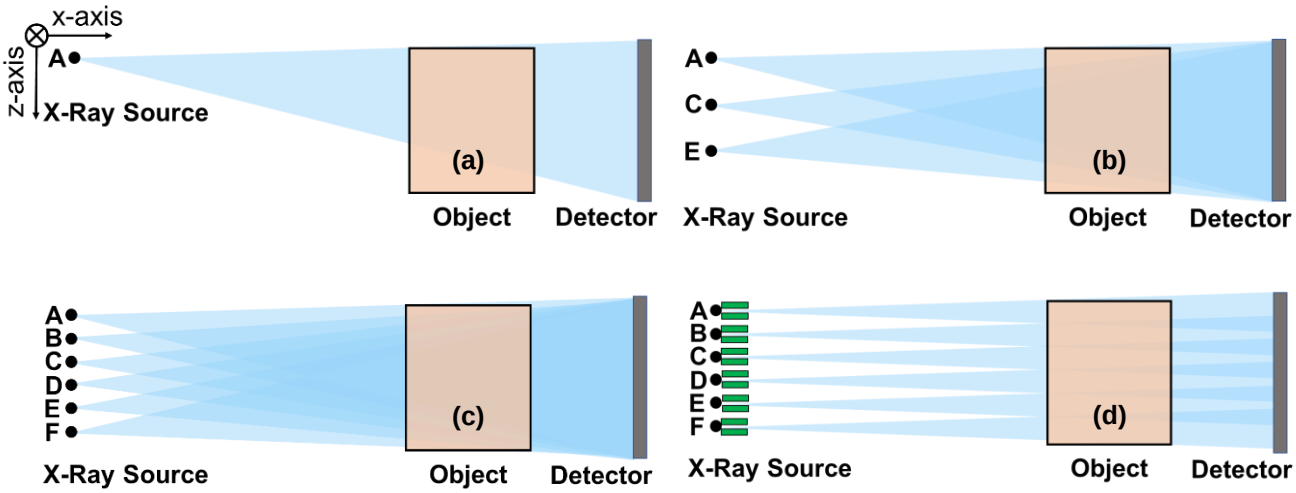

FIG 3.1. Diagrams of the geometry of each CBCT system: (a) one source, (b) three source overlapping, (c) six source overlapping, (d) six source collimated configuration. The narrow collimators are indicated in green. The blue indicates the spatial distribution of the x-ray beams. The position of each source location is constant across the different geometries. Drawn to relative scale for a source to isocenter distance of 500 mm, source to detector distance of 700 mm, detector height of 200 mm, sources separated by 30 mm in the z-dimension, and an object space of 153.6 x 153.6 x 180 mm.

3.2.2. CBCT system parameters

To illustrate various x-ray source configurations in CBCT, phantom imaging was performed on a prototype breast CBCT system "Doheny" built at UC Davis. The relevant parameters are described here, but the complete system parameters are reported elsewhere[23]. Doheny was designed as an approximate half cone system rather than a full cone system to maximize chest wall coverage for imaging the breast in the pendant geometry. The central ray is positioned near the chest wall with a maximum fan angle of 23.8°. Multiple scans using a one source x-ray tube were used to simulate a multiple-source CBCT system. A vertical actuator controlled by a stepping motor was used to move the one source x-ray tube to different vertical positions between scans and a full 360° CT

acquisition was acquired at each position. A full set of projection data were acquired producing 500 projections at each of the source positions (A-F as shown in Figure 1). Individual projections were subsequently interleaved during image reconstruction to simulate a multisource x-ray tube system as detailed in Section 2.B.2. All scans in this study were acquired with 500 projections at 60 kV with 0.2 mm Cu filtration, 150 mA, an x-ray pulse width of 4 milliseconds (ms), and a pulse period of 23 ms. This system operates with a tungsten anode x-ray tube and a nominal focal spot size of 0.3 x 0.3 mm. The tube current time product was therefore 300 mAs (150 mA x 4 ms x 500) for all the datasets in this study.

3.2.3. Image reconstruction

The volume datasets were reconstructed using the Feldkamp-Davis-Kress (FDK)[68] 3D filtered back projection with a Shepp Logan apodization filter which was implemented in MATLAB using voxel-based back projection. Each volume data set was reconstructed using an isotropic voxel size of 150 µm and a matrix size of 1024 × 1024 × 1200 voxels which creates a FOV of 150 × 150 × 180 mm. In a previous study conducted on this system[23], the system modulation transfer function

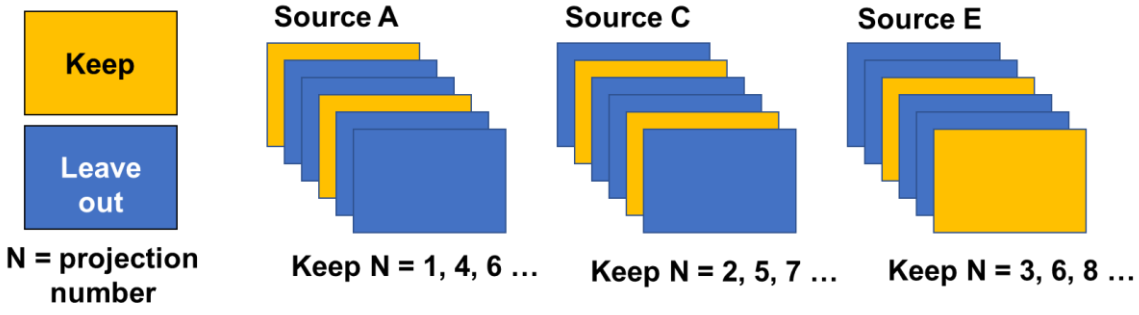

FIG 3.2. Diagram detailing the method used for image reconstruction for the overlapping multisource configurations which involves selecting a subset of each full acquisition to interleave into a combined reconstruction. An example for the overlapping three source configuration is shown.

(MTF) was measured and the 10% MTF resolution limit was determined to be 3.33 mm^{-1}, which corresponds to a voxel size of 150 μm.

For all overlapping multisource geometries, the total tube time current product used to generate each reconstructed volume dataset was kept the same by interleaving a total of 500 projections. This was achieved by interleaving a subset of the original projections from each source, demonstrated in Figure 3.2. Due to the built-in collimation of the x-ray tube housing, some of the projection data was lost when the x-ray source was moved from the original "A" position. This was accounted for by linearly scaling each voxel value after reconstruction based on how many sources contributed to it. Rigid registration was applied for the overlapping multisource geometries.

For the collimated six-source multisource geometry, a narrow collimator was applied to limit the x-ray beam to a smaller region in the z-dimension for each source position (see Figure 3.1D) and all 500 projections from each acquisition were used in the image reconstruction. These

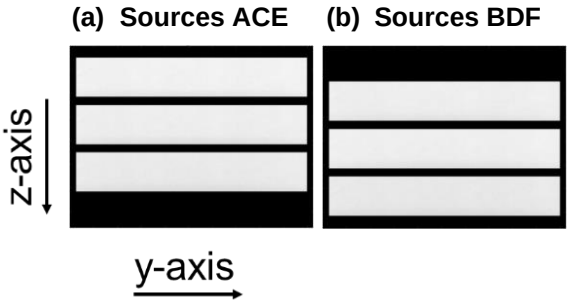

FIG 3.3. The detector (Varex Dexela 2923 CMOS) coverage applied for the collimated six source geometry. (a) coverage for sources A, C, E digitally combined. (b) coverage for sources B, D, F digitally combined. Each source covers 330 rows which equates to 49.5 mm on the detector and a 2-degree cone angle both posteriorly and anteriorly.

volumes were reconstructed into sub-volumes using the same FDK method as the one source configuration and all sub-volumes were combined in the CT image domain to complete the image reconstruction. Figure 3.3 shows the regions that were used in the collimated six-source multisource reconstruction, although the physical collimation is slightly larger than that in the diagram. In a fully assembled system, the collimation for each source would be designed precisely for the region on the detector used in the reconstruction. The coverage is contained within 1330 detector element "dexel" rows resulting in 20 cm of vertical detector coverage from the inherent collimation on the system. These exact rows were not optimized for this preliminary study. The same total region on the detector (i.e., 20 cm vertical detector coverage) was used for the one source and the overlapping multisource configuration reconstruction.

3.2.4. Defrise phantom

To demonstrate cone beam artifacts in the experimental studies on the Doheny scanner, a Defrise phantom (Fig 3.4a) was built from evenly spaced compact disks. The phantom is composed of 120 mm diameter polycarbonate disks 1.2 mm thick and evenly spaced using nylon plastic disks which are 25 mm in diameter and 2.4 mm thick. The overall height of the stack was 150 mm which is large enough to fill the entire object space. All four source configurations were used to image the Defrise phantom and compare line profiles through the 3D reconstructions. The modulation of the Defrise disks was determined by finding the difference between the maximum (95th percentile) and minimum (5^{th} percentile) within the line profile data.

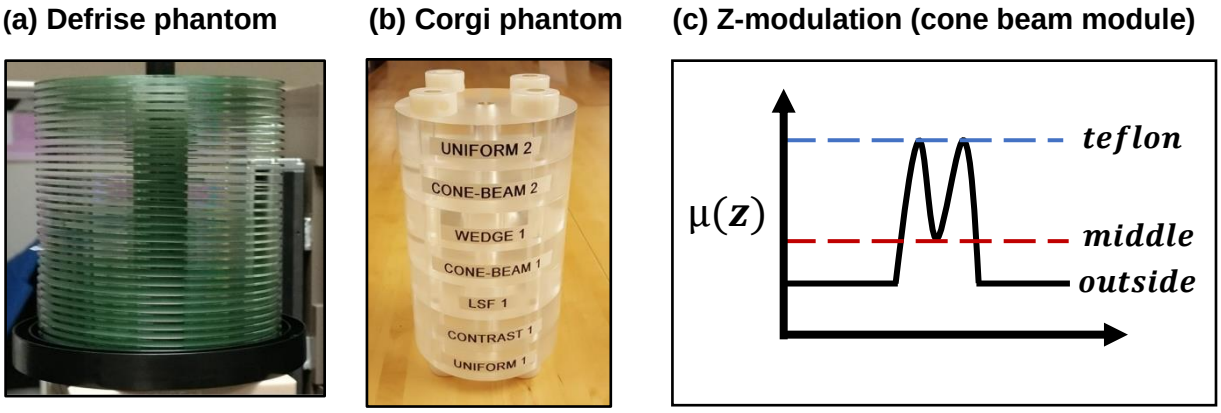

FIG 3.4. Photos of the (a) Defrise phantom and the (b) Corgi phantom used in the quantitative experimental study. (c) Line pair demonstration to show the calculation of the loss in modulation in the z-dimension (z_{mod}) through the volume data set of the Corgi phantom cone beam artifact module.

3.2.5. Corgi phantom

A multi-purpose and modular quality assurance phantom[69] for cone beam scanners was recently developed and commercialized, referred to as the Corgi phantom (Fig 3.4b). Contained within this phantom is a cone beam artifact module consisting of Teflon disk pairs separated with polyethylene terephthalate and positioned vertically in the phantom at different cone angles. The diameter of each disk is 25.4 mm with a thickness of 1.0 mm, and the disks are spaced 3.0 mm apart vertically. For these experiments, four cone beam modules were positioned 30 mm from each other vertically within the phantom and used to quantify the magnitude of the z-axis modulation at these four regions of the reconstructed FOV. The modules were positioned vertically from the one source central ray location at 30 mm, 60 mm, 90 mm, and 120 mm to isolate specific cone angles within the scanner FOV. A metric[69] has been developed for evaluating the magnitude of the

cone beam artifact referred to as the z-modulation [$\boldsymbol{z_{mod}}$] which is illustrated in Figure 4c and defined in Equation 3.1.

$$\boldsymbol{z_{mod}} = \frac{\mu_t - \mu_m}{\mu_t - \mu_o} \tag{3.1}$$

where the mean reconstructed voxel value (μ**;** linear attenuation coefficient) is measured in the Teflon (t) disk, in the middle (m) region between the two Teflon disks, and the outside (o) region beyond the disks as depicted in Figure 3.4c. When the module is completely resolvable, the [$\boldsymbol{z_{mod}}$] will approach unity and when it is completely unresolvable, the [$\boldsymbol{z_{mod}}$] will be nearly zero. To calculate the μ_t, μ_m, and μ_o values, an ROI (9 mm × 9 mm) was averaged within each coronal slice to reduce noise in the estimation.

3.2.6. Noise power spectra

It is well known in CBCT that the 3D noise power spectrum (NPS) has a null cone[70,71] that corresponds to the frequencies missing in the data and the cone angle used in the scan. This missing cone can be explained by the central slice theorem. For a single projection, the diverging rays in a cone beam tilt the 2D Fourier plane in the projection domain, which tilts the 3D Fourier plane in the reconstructed domain. Since all the projections are summed into the reconstruction, the many tilted 2D Fourier planes result in a cone shape in the reconstructed 3D Fourier domain. To characterize the noise properties and quantify the null cone, the 3D NPS was measured for the one source, three source, and six source configurations. Two identical scans of a polyethylene cylinder were reconstructed, and the data sets were subtracted to obtain a single noise-only image. The 3D $\boldsymbol{NPS}(\boldsymbol{u}, \boldsymbol{v}, \boldsymbol{w})$ was then calculated using the noise-only image with 100 overlapping volumes of

interest (VOI) centered around a circle at half the radial distance of the polyethylene cylinder. A cylinder with a diameter of 154.2 mm was used in the acquisition, so the center of the VOIs were located at 38.1 mm from the isocenter and each volume was 128 × 128 × 128 voxels.

$$\boldsymbol{NPS(u,v,w) = \frac{1}{N}\sum_{i=1}^{N}\frac{|DFT_{3D}(VOI_i(x,y,z))|^2}{2}\frac{\Delta x}{N_x}\frac{\Delta y}{N_y}\frac{\Delta z}{N_z}} \quad (3.2)$$

In Equation 3.2, the 3D frequency domain is represented by variables $(\boldsymbol{u,v,w})$ and the corresponding 3D spatial domain is represented by variables $(\boldsymbol{x,y,z})$. The $\boldsymbol{VOI_i}$ term is the individual cube of data within the difference data and the $\boldsymbol{N}$ term refers of the number of VOIs, which in this case is 100. The VOIs are 3D discrete Fourier transformed ($\boldsymbol{DFT_{3D}}$), magnitude squared, and divided by two to account for the doubling of the noise magnitude during the subtraction step. The data from 100 VOIs were averaged and then scaled by the number $[\boldsymbol{N_x, N_y, N_z}]$ and size $\boldsymbol{[\Delta x, \Delta y, \Delta z]}$ of the voxels.

In order to quantify the null cone of the 3D NPS, the elements that were less than 10% of the 95th percentile of the entire 3D NPS were classified as the null elements[47]. This criterion was used to determine the null elements within the 3D NPS and the fraction of the total that were null for each multisource configuration. The percent null elements were plotted with respect to the z-dimension relative to the central ray for sixteen regions down the length of the data. This was done in the same regions for the one source, overlapping multisource, and collimated multisource configurations.

3.2.7. Anthropomorphic phantom imaging

An anthropomorphic hand phantom measuring 25 mm × 110 mm × 200 mm and an anthropomorphic knee phantom measuring 150 mm × 150 mm × 250 mm were scanned to show the subjective differences in image quality for two simple clinical imaging tasks. The same scan protocol that was previously described was applied using the one source configuration and the collimated six source configuration.

3.2.8. Monte Carlo simulation model

A validated Monte Carlo-based radiation transport code[72] (MCNP6 version 1.0) was employed in this study to simulate: (1) primary and scatter contributions to projection images, and (2) three-dimensional dose distributions for the various source configurations. For all simulations, a 60 kV polyenergetic source with 0.2 mm Cu filtration was modeled using TASMICS[73] and implemented in MCNP6 as a probability density function for the photon source distribution. The source was defined as a point with photon emission directed towards a simulated collimation window for either the overlapping or collimated geometry as shown in Figure 1 and detailed in section 2A. A phase space file was recorded for all photons passing through the collimator window using the source surface write (SSW) card in MCNP which records each photon energy, direction, and location. The phase space files were then used with the source surface read (SSR) card in MCNP to define the source for subsequent simulations detailed in the following two sections. A separate phase space file was recorded for all six sources in the overlapping geometry. Given the symmetric collimation (in z) for the collimated geometry, only a single-phase space file was generated and then translated (using the TR card in MCNP) in z to simulate all six sources. A 154.2 mm diameter

polyethylene cylinder was modelled as a voxelized phantom 40 cm in length with an isotropic voxel size of 0.12 mm and centered about the scanner isocenter in x-y and the center of the detector FOV in z. This cylinder diameter matches that used in the NPS measurements in the experimental study. The excess phantom length beyond the 14.4 cm detector FOV was simulated to include the effects of backscatter.

For normalization of the projection image and dose simulations, the air kerma free-in-air was simulated at the isocenter by modelling a 0.6 cm^3 thimble ionization chamber (10x6-0.6CT, RadCal Corp., Monrovia, CA, USA). A total of 6.0 × 10^8 and 1.3× 10^9 photons were tracked and written to the phase space files for the collimated and overlapping geometry, respectively. This number of source photons was sufficient to ensure that the relative error was less than 1% across all projection, dose, and air kerma simulations.

3.2.9. Primary and scatter contributions to projection images

For simulation of projection images, the detector geometry detailed in section 2B was modeled in MCNP6. An ideal energy integrating detector model was implemented in the simulations which assumes 100% absorption efficiency of photons independent of detector material and incident angle46. The estimated scatter-to-primary ratio (SPR) from this model is within ~5% of measured values for the photon energy range investigated in this work providing confidence that this detector model is suitable for the purpose of this work. Simulation of the native dexel pitch (0.075 mm) for the flat panel detector utilized in this work is superfluous for the purpose of comparing the primary and scatter contributions across the different source configurations. Moreover, the scatter contribution to projection images is a relatively low frequency effect and does not require high resolution simulations for accurate estimation. Therefore, the primary projection images were simulated with a dexel pitch of 0.75 mm using a grid of point detector tallies (*F5 in MCNP6),

after correcting for the surface area of each dexel and the cosine of the angle between the primary x-rays and the normal to the detector surface[74]. The scatter projection images were simulated with a dexel pitch of 3.75 mm using a grid of point detector tallies (*F1 in MCNP6) which records the energy current through the detector surface using a modification card to discriminate between primary and scatter contributions. Lastly, the low-resolution scatter projections were interpolated to match the resolution of the primary projections and then used to calculate the scatter-to-primary ratio across the entire detector surface. The primary, scatter, and SPR projections were compared across the different source configurations investigated in this work. The simulated air kerma (mGy per source particle) was scaled to the detector surface using the inverse square law and used to normalize all projection images (MeV per source particle) such that each dexel is in units of MeV per mGy at the detector surface.

3.2.10. Three-dimensional dose distributions

The energy deposited per unit mass (MeV/g) was estimated for each voxel within the voxelized polyethylene phantom (F6 in MCNP6) and converted to units of dose (mGy) by multiplying the tally output by 1.6022 × 10^(-7). Three-dimensional dose distributions were simulated for all six sources in both the collimated and overlapping geometry (12 total simulations). All dose distributions were then divided by the simulated air kerma at the isocenter such that the unit of each voxel is absorbed dose per air kerma (mGy/mGy). Given that the cylindrical phantom is homogenous and symmetric about the scanner isocenter, separate simulations were not required for rotating the phantom (or source). Phantom rotation was accomplished by bilinear interpolation of the 3D dose distribution for a single projection through any arbitrary rotation angle, ensuring that the rotated dose map was the same size as the original dose map. This approach to estimating

the dose distribution for an entire CBCT scan allows for flexibility in simulating any arbitrary number of rotation angles, orbital extent, source configuration, and source exposure sequencing.

3.3. Results

3.3.1. Defrise phantom

The results from the Defrise phantom for the various source configurations are shown in Figure 3.5. A single sagittal slice through the center of the reconstructed volume data set shows qualitative differences between the source configurations. An arrow is superimposed onto each image to show where data was extracted for a line plot from the top to bottom slices. Line plots were created to quantify the cone beam artifacts. A region of 2 x 2 pixels in the coronal plane was averaged for each slice of the line plot to reduce noise. When the one source configuration was used to image

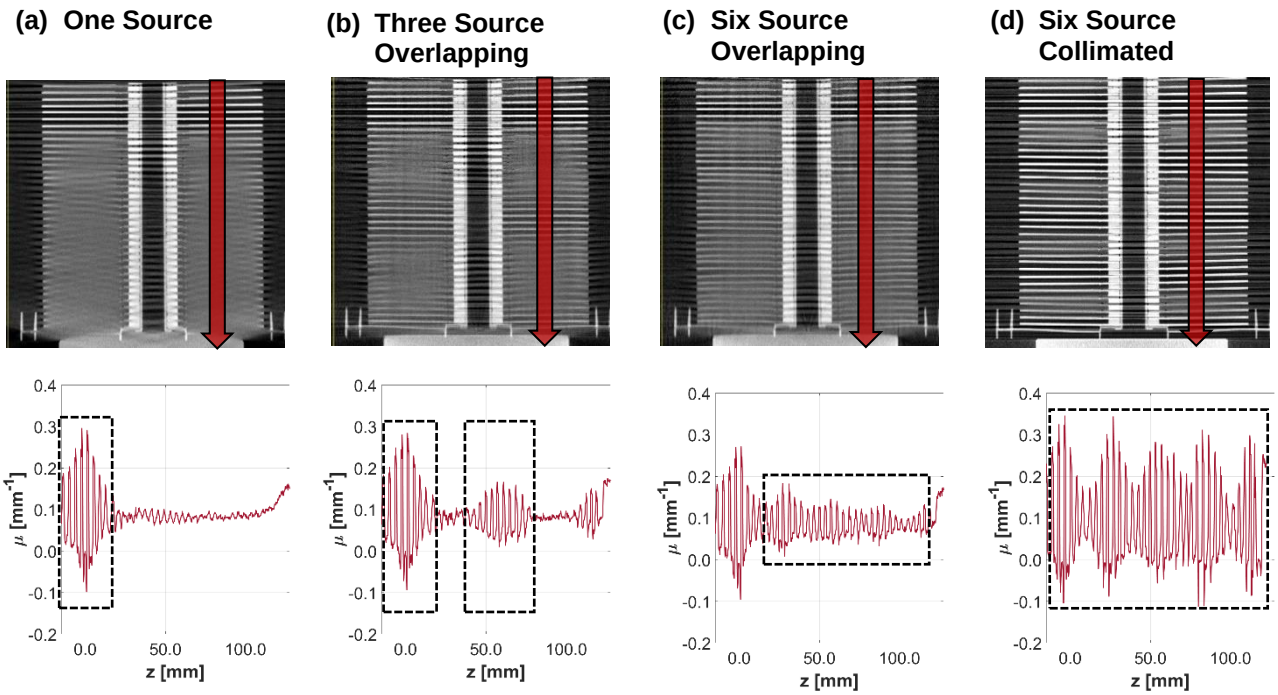

FIG 3.5: Defrise phantom results are shown for the (a) one source, (b) three source overlapping, (c) six source overlapping, and (d) six source collimated configurations. Sagittal slices through the reconstructions are shown in the top row qualitatively demonstrating modulation of the disks and the bottom row shows line plots through the volume quantifying the modulation.

the Defrise phantom, the disks are distinguishable for only a small region of the total FOV, about 30 mm in the vertical direction near the central ray of the x-ray beam. The same trend is apparent in the three-source overlapping configuration, where the visibility of the disks is improved near each of the central rays of the x-ray beam. The six-source overlapping configuration resolves the disks for the entire phantom, however a considerable fraction of the modulation intensity is lost. The modulation of the disks on average throughout the volume is 2.7X greater for the six-source collimated configuration than the six-source overlapping configuration. The six-source collimated configuration uses only the small cone angle ($\theta = \pm 2°$) projections from each source to the object, resulting in nearly full modulation intensity throughout the entire phantom.

3.3.2. Corgi phantom

A sagittal slice through the volume data of the Corgi phantom with the cone beam factor modules is displayed in Figure 3.6 alongside line profiles of the data measured orthogonal to the disk planes. This line profile data was used to calculate the modulation in z (Figure 3.4) for four positions within the scanner FOV (in z) as shown in Figure 3.7.

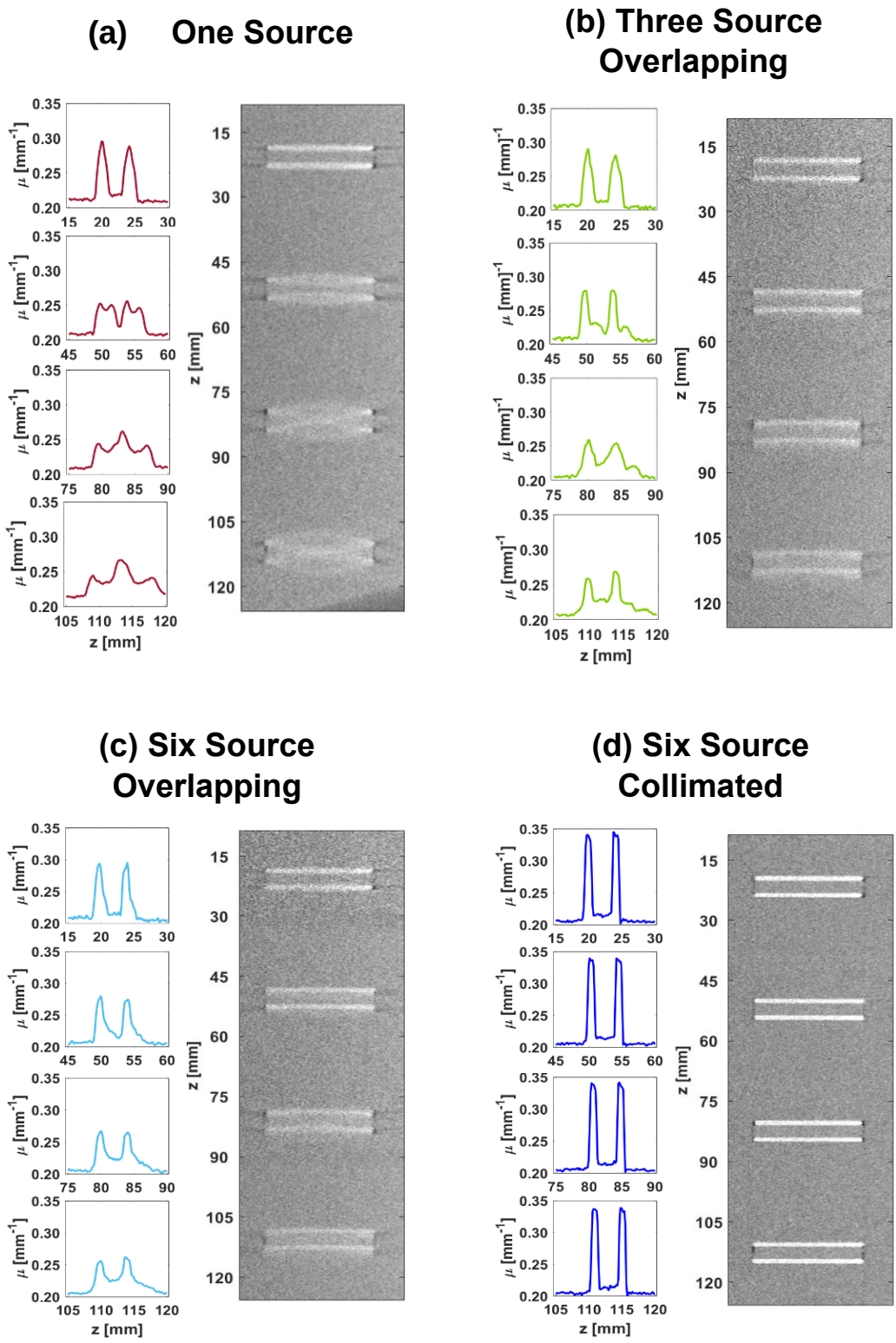

FIG 3.6: Cone beam modules from the Corgi phantom used to evaluate the modulation in z at various vertical locations throughout the object space. Each row of data corresponds to a position in the z-dimension relative to the central ray displayed on the right.

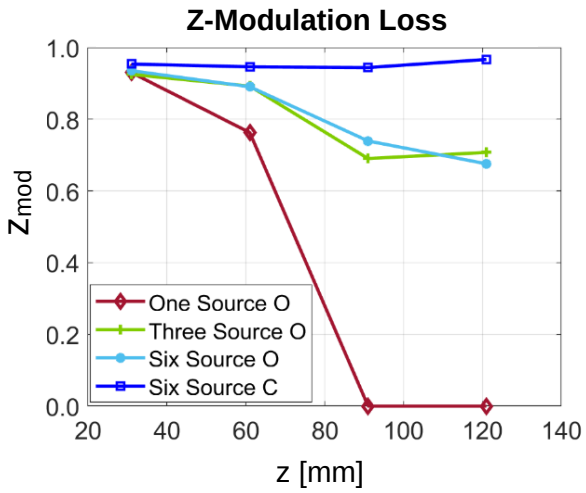

FIG 3.7. Cone beam artifact measured as the loss in modulation in the z-dimension for several multisource systems compared to the one source system for four locations along the z-dimension relative to the central ray. Four configurations are represented: one source, three source overlapping, six source overlapping, six source collimated. In the legend, O = overlapping and C = collimated.

3.3.3. Noise power spectra

An example of a central slice through the 3D NPS is illustrated in Figure 3.8 for all four configurations to show the null cone. This example captures the NPS in a volume of interest that is between 107.2 to 126.4 mm in the z-dimension. For the one source configuration, this corresponds to the region between 12 to 14 degrees cone angle. It is displayed in a cropped window to feature the null cone and not the apodization of the ramp filter.

The cone angle was measured from a central slice of the 3D NPS (as shown in Fig 3.8a) as the half angle within the null cone. To validate this method, the measured cone angle within the null cone map was compared to the true system cone angle from the geometry of the one source configuration. The measured cone angle and true cone angle were plotted and found to have a coefficient of determination equal to 0.99 showing that the criterion could correctly identify the

null elements within the 3D frequency domain. The fraction of the elements within the 3D NPS that were null was tallied for seventeen positions through the z-dimension and are plotted in Figure 3.9.

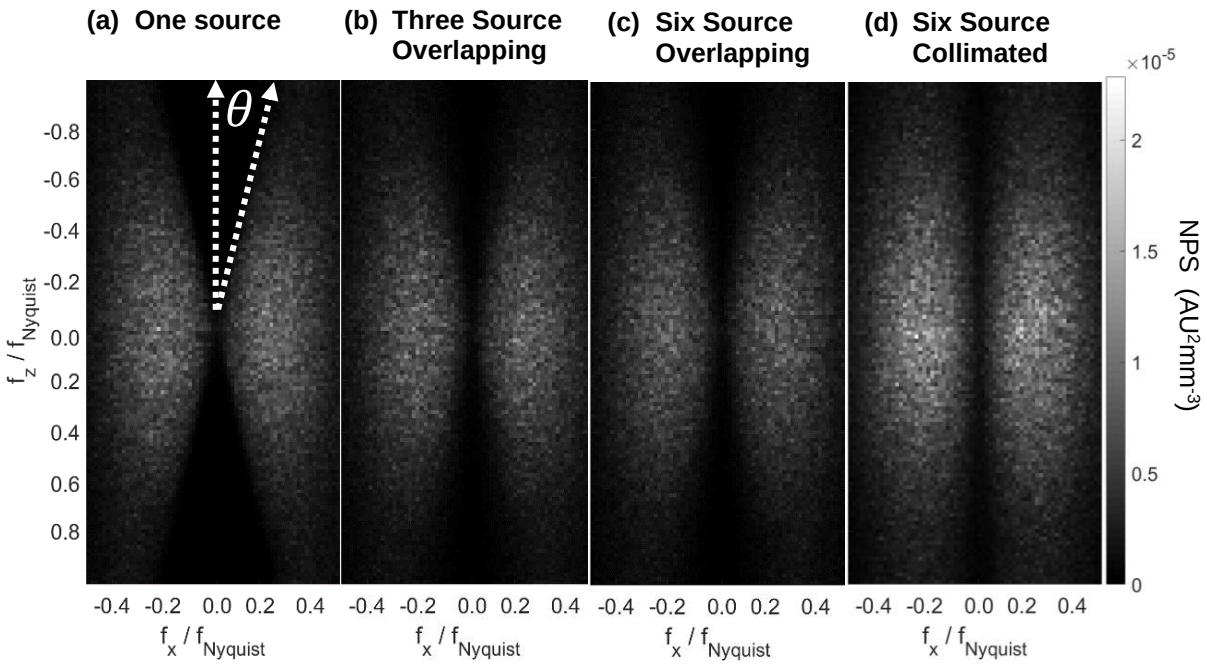

FIG 3.8. Sagittal slices though the 3D NPS for the four different MXA configurations at a cone angle of 14 degrees (relative to one source) to illustrate the null cone recovery in the multisource systems. (a) one source configuration with an illustration of the null cone measurement, (b) three source overlapping configuration, (c) six source overlapping configuration, (d) six source collimated configuration.

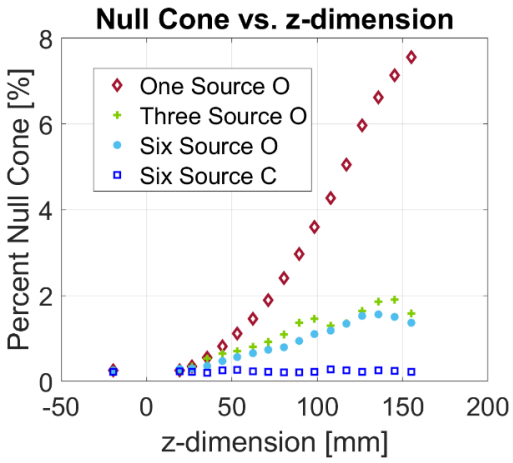

FIG 3.9. Percent null cone within the 3D NPS plotted at sixteen locations through the field of view. Four configurations are represented: one source, three source overlapping, six source overlapping, six source collimated. In the legend, O = overlapping and C = collimated.

3.3.4. Anthropomorphic phantom imaging

A slice through the reconstructed volumes was used to visualize the differences in the hand (Fig 3.10) and knee (Fig 3.11). A sagittal slice is displayed to show that the one source configuration cannot recover the entire field of view (Figure 3.10a) while the collimated multisource configuration (Figure 3.10c) extends the field of view to capture the full length of the hand. A small region of the hand is selected from the image between 55 to 85 mm from the central ray in the one source system because it is positioned at a large cone angle and the qualitative difference in anatomical details is revealing. These improvements in image quality for the six-source collimated configuration are due to both a reduction in the cone beam artifacts (Figure 3.7) and a reduction in scatter contamination (discussed in the following section).

Between the metacarpophalangeal joints there are apparent streak artifacts when the one source configuration was used. Figure 3.11 shows a coronal slice from the knee phantom data positioned at 80 mm from the central ray to illustrate the difference in contrast to noise between

the one source configuration (Figure 3.11a) and the collimated six source configuration (Figure 3.11b). In both anthropomorphic phantoms, the details within the bone structure are obscured when one source is applied, and they are much sharper when the collimated small cone angle configuration is applied. The visibility of these fine structures can impact the diagnostic quality of CBCT scans for many orthopedic applications, as discussed in the introduction of this chapter.

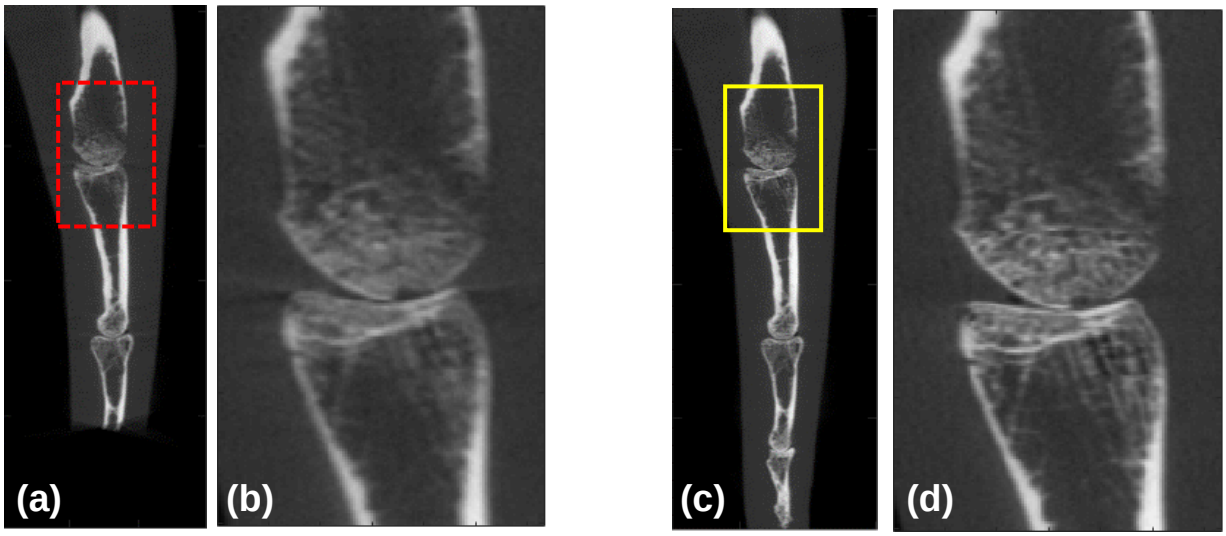

FIG 3.10: Anthropomorphic hand phantom scanned by both the one source system and the collimated six source system. Sagittal slices are shown through the reconstructed volumes with a region of interest. (a) one source system full FOV, (b) one source system ROI FOV, (c) six source collimated configuration full FOV, (d) six source collimated configuration ROI FOV. The slices were displayed with the same window range of attenuation coefficients [0, 1.2] mm^{-1}.

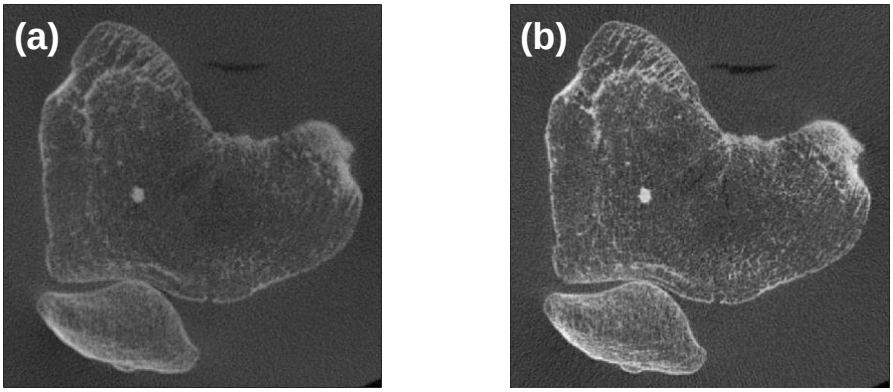

FIG 3.11: Anthropomorphic knee phantom scanned by both the one source system and the collimated six source system. Coronal slices are shown through the reconstructed volumes at 80 mm from the central ray, which corresponds to a cone angle of 9° in the one source configuration. (a) one source configuration (b) collimated six source configuration. The slices were displayed with the same window range of attenuation coefficients [0, 0.9] mm^{-1}.

3.3.5. Primary and scatter contributions to projection images

The signal to primary ratio (SPR) simulated at the detector surface for the collimated and overlapping configurations is shown in Figure 3.12. A 2D map of the SPR for the collimated one source configuration and the overlapping one source configuration is shown. A subset of the 2D SPR maps was extracted to quantify the SPR along z (Figures 3.12 c-d) by calculating the mean SPR for all dexels within an ROI (1 cm × 1 cm) centered about the z-locations indicated in the figure. Two sets of ROIs were considered, one at the center of the detector columns "central" and another at the periphery of the columns "peripheral" which was set at one quarter of the detector width. The specific z locations of the ROIs were chosen to align with the center of the collimated FOV for each source. The maximum SPR was determined by calculating the 95^{th} percentile of the 2D SPR map (Figure 3.12 a-b) within the shadow of the phantom on the detector. The maximum SPR for the collimated configuration was 0.26 while the maximum SPR for the overlapping

configuration was 0.81. The scatter distribution was compared between the overlapping and collimated configurations for source A and source F, shown in Figure 3.13. This plot was created by collecting ROIs (1 cm × 1 cm) on the detector to calculate the mean scatter at each row position.

The summation of simulated scatter distributions for collimated sources A, C, E and the summation of collimated sources B, D, F were also compared for a theoretical multisource configuration which utilizes simultaneously triggered sources (labeled “ACE collimated” and “BDF collimated” in Figure 3.13). The collimated multisource configuration theoretically allows for simultaneous source activation as illustrated in Figure 3.3 for two consecutive projection images. This is unique to the multisource collimated geometry because there is no overlap of the primary beam from a subset of sources on the detector. In this configuration, sources A, C, E could theoretically be triggered simultaneously and sources B, D, F could also be triggered simultaneously. However, given that the Doheny scanner used in the present experiments does not have the multisource x-ray tube installed, simultaneous triggering is not possible. In the experimental study, only one source was triggered at a time, and a narrow collimation scheme is used to limit the exposure to a sub volume within the total field of view. In a system that is triggered simultaneously, there would be an increase in scatter contamination from adjacent sources (as illustrated in Figure 3.13) that would need to be considered. Simultaneous source triggering is discussed further in section 3.4.2.

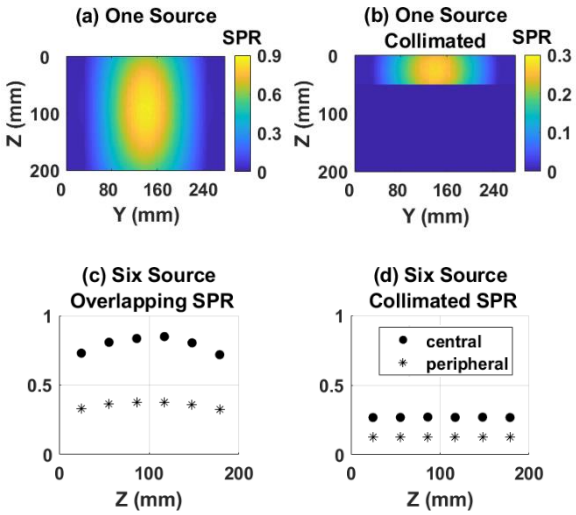

FIG 3.12. Top row: Monte Carlo simulation results showing 2D maps of the scatter to primary ratio (SPR) on the detector surface for a 154.2 mm polyethylene cylinder scanned using one source position 'A' in the (a) overlapping configuration and the (b) collimated configuration. One dimensional SPR profiles along the z (rows) of the simulated detector in the (c) six source overlapping configuration and the (d) six source collimated configuration is also shown. The central ROIs were centered about y = 139 mm and peripheral ROIs were centered about y = 69 mm. Along the z dimension, the ROIs (central & periphery) were centered about z = 25, 55, 85, 115, 145, and 175 mm.

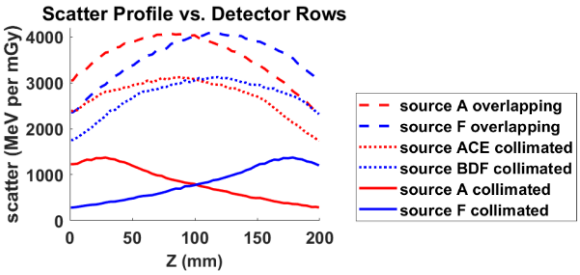

FIG 3.13. Line profile down the detector rows at the center of the columns Y(mm) = 139 to show the magnitude of the scatter distribution for source A and source F in both the collimated and overlapping configurations. The simulated air kerma (mGy per source particle) was used to normalize the projection images (MeV per source particle) to calculate the scatter (MeV per mGy) plotted here.

3.3.6. Three-dimensional dose distributions

The average and maximum dose (95th percentile) for the four different source configurations were calculated from the Monte Carlo simulation results and detailed in Table 3.1. A sagittal slice through the center of the 3D dose distributions for the different source configurations are shown in Figure 3.14. Each dose map is normalized to the maximum dose and displayed on a scale from 0 to 1 to show the relative dose distributions. Line profiles (along z) through the 3D dose distributions are also shown in Figure 3.14. An ROI (1 cm × 1 cm) was averaged across the coronal plane of the volume to calculate the data for the line profiles at the center and periphery (1.5 cm from the edge of the phantom) of the 3D dose distributions. The profiles for the overlapping configurations were plotted on a scale from 0 to 3 mGy per 100 mAs while the collimated configuration was plotted from 0 to 1.5 mGy.

Table 3.1. Monte Carlo dosimetry metrics for the various multisource CBCT configurations

Metric	**One Source**	**Three Source Overlapping**	**Six Source Overlapping**	**Six Source Collimated**
Number of projections per source	498	166	83	498
Dose, average (mGy/100 mAs)	2.098	2.256	2.259	0.513
Dose, maximum (mGy/100 mAs)	2.864	2.827	2.823	0.640

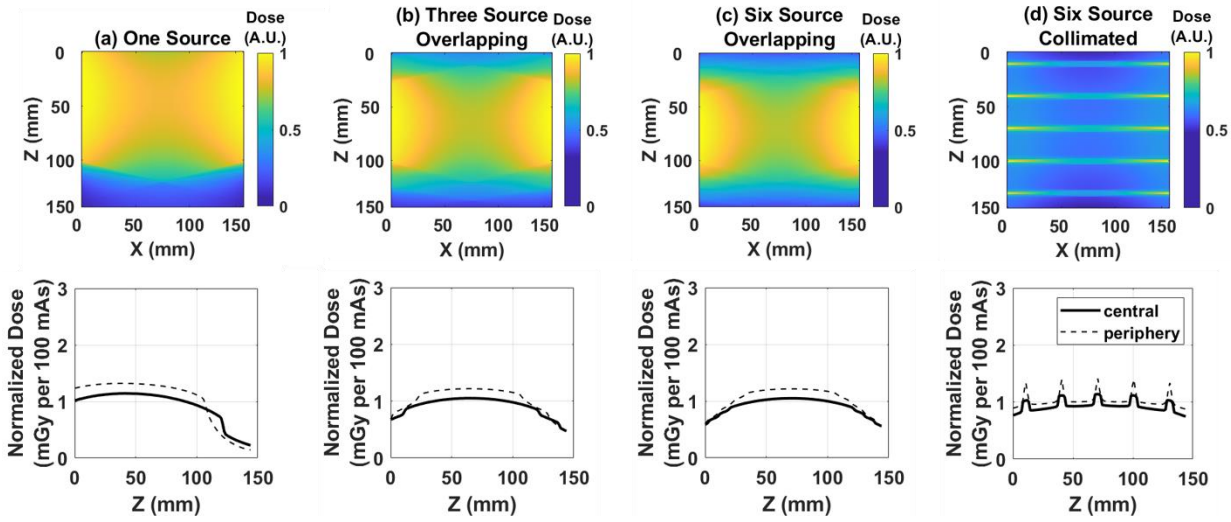

FIG 3.14. Top row: central slices through the 3D dose distributions for the various multisource configurations, each normalized to the maximum dose within the corresponding volume. Bottom row: line profiles through the 3D dose distributions at the center and periphery of the volume, each normalized to the average dose within the corresponding volume.

3.4. Discussion

3.4.1. Experimental study

The phantom imaging studies presented in this work demonstrate the image quality improvements and utility of the multisource concept applied to cone beam CT. The Defrise phantom and the Corgi phantom quantify the variable contrast modulation throughout the scanner FOV, and the null cone in the 3D NPS quantifies the missing frequencies throughout the scanner FOV. Within the FOV of the one source configuration, the farther the position is from the central ray, the more information is lost in both the spatial and frequency domains. The collimated six source configuration shows the most improvement for all three phantom studies when compared to the one source configuration. These two configurations were then used to image the two anthropomorphic phantoms (Figures 3.10 and 3.11) and demonstrated clear qualitative differences

in the contrast with the collimated six source configuration providing significantly improved visibility of fine details. The smaller sub volumes in the collimated geometry contribute to a decrease in the noise caused by scattered photons and essentially eliminates cone beam artifacts because only small cone angles are used during the acquisition. One limitation of the study was that the built-in collimation of the x-ray tube prevented the full coverage of the detector for the overlapping geometries. This implies that the volume datasets from the overlapping geometries have inconsistent noise properties throughout the field of view.

3.4.2. Monte Carlo simulation

The Monte Carlo simulation results demonstrate the differences in the scatter contributions between the collimated and overlapping geometries. For a full FOV (overlapping geometry), the SPR varies down the length of the detector with a peak at the middle of the polyethylene phantom (Figure 3.12c). In the collimated geometry configuration, the SPR remains consistent down the length of the detector (Figure 3.12d). The scatter interactions were examined separately from the primary interactions and compared between the overlapping and collimated configurations (Figure 3.13) for the top “A” and bottom “F” source positions. The magnitude of the scatter is greatly reduced when comparing the overlapping to the collimated source configurations at the same source positions. When only one source is triggered at a time, the scatter is limited and does not depict the scatter that would occur for simultaneously triggered sources that was discussed as a potential benefit of the multisource collimated geometry (but not physically simulated on the breast CT scanner used in this study). Monte Carlo simulation comparisons with simultaneous triggering of multiple collimated sources are also shown in Figure 3.13 (labeled “ACE collimated” and “BDF collimated”) demonstrating an increase in scatter contamination in the projection domain from adjacent sources as expected.

Simultaneous triggering of multiple sources in the collimated multi-source configuration would however provide a higher duty cycle and therefore make more efficient use of the scan time and improve angular sampling. The duty cycle refers to the fraction of the time within a complete acquisition that an individual source is active. For example, consider a single source (non-simultaneous) acquisition with 6 sources and a total of 498 projections acquired in 360 degrees. Each source would be active in only 1/6 or equivalently 83 of the 498 projections. With simultaneous pulsing (3 sources at a time) and an odd (A,C,E) / even (B,D,F) synchronization approach, each source would contribute to ½ or equivalently 252 of the 504 projections. Hence the duty cycle would increase from 1/6 (0.17) to ½ (0.5) with an increase of a factor of 3.

The 3D dose distributions show that the maximum dose for all the overlapping configurations (one, three & six) remained relatively constant, but the average dose for the multisource (three & six source) overlapping configurations had increased 25% when compared to the one source configuration. This increase in the average dose can be attributed to the improved coverage of the phantom volume near the bottom of the FOV when multiple sources are used as shown in Figure 3.14b & 3.14c. There is a four-fold decrease in both the average dose and the maximum dose when comparing the collimated six source configuration and all the overlapping configurations. These results are as expected since the multisource, collimated geometry makes more efficient use of the x-ray beam by not irradiating the object at large cone angles which effectively mitigates cone beam artifacts and reduces scatter contamination in the projection domain as demonstrated in this study. While these results are promising there is a need to optimize the system geometry for the multisource collimated configuration to minimize hot spots in the dose distributions (shown in Figure 3.14d) and reduce total scan times by investigating more complex source and detector synchronization schemes.

3.5. Conclusions

Multisource CBCT configurations were physically simulated and evaluated based on image quality in the spatial domain, sampling in the frequency domain, radiation dose, and scatter contributions. The multisource overlapping configurations reduced cone beam artifacts and improved frequency sampling relative to a single source configuration, but the contrast is compromised and there is considerable scatter contribution to the signal. The collimated multisource concept applied to CBCT was shown to significantly reduce scatter (Figure 3.12-3.13) and improve consistency in image quality (Figures 3.5-3.7) throughout the FOV when compared to standard CBCT (one source). The collimated beam multisource concept also showed the reduction of artifacts and improvements in contrast in two anthropomorphic phantoms (Figures 3.10-3.11).

The combination of improved image quality and reduced dose makes the collimated six source configuration for CBCT a promising potential modality for clinical imaging. Therefore, we believe that collimated multisource CBCT applied to clinical applications has the potential to provide more consistent image quality throughout the FOV and more reliable diagnostic information when compared to standard one source CBCT.

Chapter 4: Breast CT microcalcification detectability with phantom imaging and the ideal observer

4.1. Introduction

The visualization of microcalcifications is critical for a breast cancer screening procedure. Ductal carcinoma in situ (DCIS) is a noninvasive potential precursor of invasive breast cancer[75,76] that accounts for 20–30% of all breast cancers and presents as suspicious microcalcifications in 60–90% of lesions.[77,78,79] It has been shown in clinical trials at UC Davis that dedicated breast CT (bCT) is better than digital mammography (DM) at detecting masses, but that DM is better than the early generation bCT system[24] at detecting microcalcifications. This is due to several factors that affect the image quality in the reconstructed images. The noise is greater in bCT than DM due to the lower dose per projection image. For an average scan of one breast, bCT applied 500 projections at ~0.35 mAs per projection, while DM applies only 2 projections at ~50 mAs per projection. While the increase in the number of views in bCT improves the visualization of masses by overcoming the superposition of tissues, it also increases the quantum noise when compared to DM. In addition, the electronic noise is greater in bCT because the detector is operated with a much higher amplification gain. The spatial resolution of the early bCT prototype was a limiting factor that was improved in the updated bCT system[23] by smaller detector elements and a pulsed x-ray tube.

The visibility of malignant microcalcifications was improved in clinical trials[80,81] by using contrast enhanced breast CT due to the uptake of contrast agent. However, the injection of contrast makes this imaging procedure more invasive and not practical for breast cancer screening for the

normal risk population. For non-contrast breast CT to be used clinically for breast cancer screening, improvements in microcalcifications detection should be made.

Previous simulation studies show the effects of detector pixel size[82], breast diameter[83], and FDK[68] reconstruction kernel[84] on breast CT microcalcification detection. Phantom studies show the effects of tube potential and radiation dose[85] on the detection of microcalcifications by human observers on a prototype system. Studies using clinical datasets at UC Davis show the utility of the ideal observer model[86] and human observer[87] for studying the effect of slice thickness on mass lesion detectability in breast CT, but these did not include microcalcification lesions.

The study herein reports on the development of a physical breast phantom with microcalcification lesions for evaluation of a prototype breast CT scanner using model observers. The microcalcification detection task for breast CT evaluated using a non-prewhitening-matched filter (NPW) model. The NPW is considered the optimal detector, or ideal observer, under the assumption of a stationary Gaussian image background[88]. This provides a method for evaluating numerous scan parameters on the prototype breast CT scanner and investigation of the impact of cone angle on microcalcification detectability.

4.2. Methods

The goal of developing this phantom was to create a simple model of a microcalcification lesion within a homogeneous glandular tissue surrounded by adipose tissue in the breast. Multiple microcalcification lesions will be scanned at a time to create a set of samples to determine statistics and draw conclusions from.

4.2.1. Calcium grains

Calcium carbonate ($CaCO^3$) grains (CIRS Inc. Norfolk, VA) were used in this study as a surrogate for microcalcifications[89,90,91]. Calcium carbonate is comparable to the chemical composition of breast microcalcifications found clinically, which include calcium oxalate in the form of weddellite and calcium and phosphorus, mostly in the form of hydroxyapatite[92] or tricalcium phosphate[93]. While the attenuation coefficient of calcium carbonate is somewhat lower than these other forms of calcium, calcium carbonate is a popular choice for microcalcifications because of its availability and lower contrast that makes it more challenging to detect.

Typically, the grains are selected by capturing them between sieves of different pore diameters. This process isolates grains roughly uniform in size, although some variability in the total volume of each calcium grain is to be expected because of their oblate or prolate shape, and other irregularities. The reported size of the grains in this study was 0.212-0.224 mm, which represents a size consistent with actionable microcalcifications[94].

4.2.2. Microcalcification phantom design

The calcium grains were placed between layers of 1% agar solution in cylindrical polystyrene test tubes (1.5 cm in diameter and 6 cm in length) which in turn could be inserted within a breast-shaped phantom. Agar was chosen as a surrogate for fibroglandular tissue in the breast because it was accessible, and the density matches that of fibroglandular tissues which results in similar x-ray attenuation coefficients as measured with CT. This phantom design approximates the clinical setting where microcalcifications predominantly reside within areas of fibroglandular tissue or a mass lesion of similar density. A total of three test tubes were filled with the mixture of calcium

carbonate grains and agar. Additionally, in each test tube three Teflon spheres 2.4 mm in diameter were also embedded (one at the bottom and two at the top) for the purpose of fiducial alignment.

The breast phantom was fabricated from ultra-high molecular weight polyethylene (UHMW), which has x-ray attenuation properties like adipose tissue. The phantom size and shape parameters were determined from a cohort of 215 patient breast CT data sets[95], and the median (by volume) amongst 6 phantoms was used here. The median-sized phantom (V3) has a total volume of 614 cm^3, a vertical length (z) of 9.8 cm, a chest wall diameter of 12.5 cm, and a diameter of 10.7 cm at the vertical center-of-mass.

4.2.3. Phantom imaging

All three microcalcification phantom inserts were imaged separately in-air on both a commercial μCT system and a prototype breast CT system for generation of calcium-grain signal profiles. The three microcalcification phantom inserts were also placed within the V3 phantom background (in-phantom) and imaged on the breast CT system to demonstrate the utility of these calcium-grain profiles for microcalcification detectability under realistic clinical imaging geometry and dose levels. The microcalcification phantom inserts were imaged both individually (in-air), as shown in Fig. 4.1(a-b), as well as inserted in a well within a breast-shaped phantom background (in-phantom) as shown in Fig. 4.1(c). The arrow in Fig. 4.1(c) is pointing to a microcalcification phantom insert that is protruding from the top of the V3 phantom background. A pipette was used to displace the small air gap surrounding the test tube with water with care taken to avoid air bubbles.

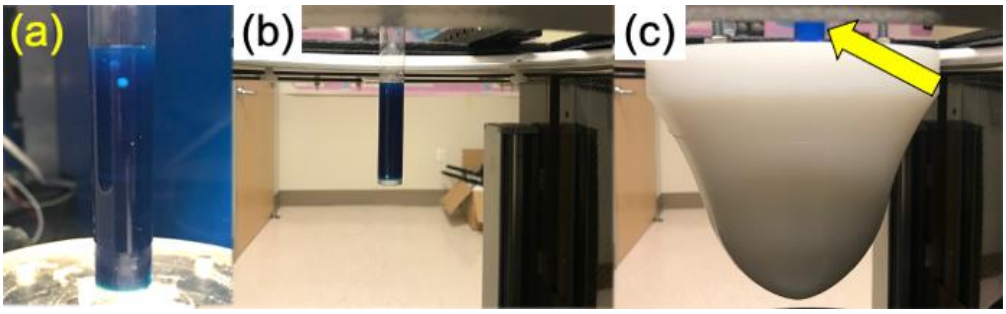

Fig. 4.1 Photographs of the microcalcification (microcalcification) phantom insert fixtured on the rotating stage in the μCT scanner (a), suspended in-air in the breast CT scanner (b), and placed within a realistic shaped, median-sized breast phantom and suspended in the breast CT scanner (c). The top of the microcalcification phantom insert is indicated by the yellow arrow in (c).

4.2.4. In-air microcalcification phantom scans with μCT

Each microcalcification phantom was first imaged on a commercial μCT system (MicroXCT-200, Carl Zeiss X-ray Microscopy) within the Center for Molecular and Genomic Imaging at UC Davis. The phantom was fixtured to a rotating platform [Fig. 4.1(a)] and 800 projections were acquired in step-and-shoot mode for a complete 360-degree rotation using a 40 kV x-ray source. A total of 6 separate scans were acquired by translating the stage 9.2 mm between consecutive scans to cover all agar within the cylindrical test tubes. The projection data were reconstructed using filtered backprojection (FBP) into a 3D volume data set with an isotropic voxel size of 0.034 mm. The characterization of individual microcalcifications using μCT and comparison with breast CT datasets are detailed in a manuscript submitted to the Journal of Medical Imaging by AM Hernandez[96], which provides the framework to calculate detectability directly from breast CT.

4.2.5. In-air microcalcification phantom scans with breast CT

The phantom was imaged on a fourth-generation breast CT scanner "Doheny" in our laboratory using 60 kV with 0.2 mm Gd filtration which was previously installed on the filter wheel. This choice of kV/filtration combination has been demonstrated to provide a good tradeoff for maximizing soft tissue and iodine contrast while still providing enough tube output within the short (4 ms pulse width) of the x-ray tube[97]. Ultra-high dose scans of the microcalcification phantom inserts suspended in-air were acquired using 800 projections in a 360-degree rotation and the maximum mA at 60 kV (860 total mAs). A total of 5 repeat scans were acquired for ensemble averaging to minimize noise. Prior to ensemble averaging, pairwise subtraction was used to verify that the phantom did not move and that the x-ray source and detector were stable during scanning.

4.2.6. Image reconstruction

For all breast CT acquisitions, the reconstruction process used a variation of the Feldkamp algorithm with a sharp Shepp-Logan kernel that cuts off at a frequency equal to two times Nyquist. An isotropic voxel size of 0.102 mm was used for reconstructions done in 1x1 binning mode and an isotropic voxel size of 0.204 mm was used for reconstructions done in 2x2 binning mode. A low-frequency shading-artifact correction was performed using a previously-reported correction algorithm[67].

4.2.7. In-phantom breast CT imaging

In-phantom imaging was performed at mean glandular dose (MGD) levels of 3 and 6 mGy in 1x1 binning mode with an x-ray pulse width of 4 ms and a total of 250 projections. MGD levels were

calculated based upon previously reported normalized glandular dose values and measured air kerma values at the scanner isocenter. The same reconstruction process explained in the previous section was used for the in-phantom images. A total of 23 repeat scans were acquired to obtain replicated images of each calcium grain for use in detectability estimation. Pairwise subtraction was used to verify stability of the imaging conditions. These scans were used for assessing microcalcification detectability performance using a non-prewhitening (NPW) matched filter model observer as explained in section 4.2.9.

4.2.8. Registration of in-air scans with in-phantom scans

Calcium grain detectability calculations required an alignment procedure to register the in-air scans with the in-phantom breast CT scans. To address template alignment, a single low-noise breast CT image of the in-phantom acquisitions was first generated by taking the ensemble average of all 23 repeat scans. The three Teflon spheres embedded in each of the microcalcification phantom inserts were used for an initial, rigid registration between the ensemble average of 5 in-air scans and the ensemble average of 23 in-phantom scans. After this initial registration, each individual calcium grain was localized in the in-air scans using a combination of Otsu's method[98] for binary segmentation and connected components analysis for distinguishing between individual grains. Three-dimensional volumes-of-interest (VOIs) centered about the binarized image center-of-mass of each individual calcium grain were then extracted from the breast CT reconstructions. Each VOI was 1.632 mm × 1.632 mm × 1.632 mm (i.e., 8 × 8 × 8 voxels for 2x2 binning mode and 16 × 16 × 16 voxels for 1x1 binning mode). All VOIs containing either more than one calcium grain or materials other than agar and calcium carbonate were excluded from the analysis. Each

template (in air) VOI was then iteratively translated and compared against the in-phantom VOI in a loop driven by minimizing the MSE computed between the VOI pairs to achieve fine alignment.

4.2.9. Detectability from the breast CT scanner

A non-prewhitening (NPW) matched-filter model[96] was used for all detectability calculations. In this model, the mean signal profile was used as a detection template. Our previous studies[99,96] compared detectability estimates derived from the μCT data with estimates derived directly from the breast CT scanner as a test of the accuracy of the results using μCT as the ground truth. However, in this study we focus on directly calculating detectability with breast CT scans only.

A 2D central profile through each breast CT-derived signal template was used as a detection template in the NPW model. Template responses are defined by an inner product of the template with an ROI from the in-phantom breast CT reconstructions. The signal-present response was computed by taking the inner product of the NPW template with the in-phantom breast CT reconstructions at the calcium grain location. The signal-absent response was computed by taking the inner product of the NPW template with the in-phantom breast CT reconstruction at 10 different non-signal locations randomly selected within the same slice and contained within the agar region of the microcalcification phantom insert. Let λ^{+}represent the signal-present template responses and $\lambda_{i,j}^{-}$ represent the signal-absent template responses, where $i = 1, \dots, 23$ indexes the 23 repeat scans and $j = 1, \dots, 10$ indexes the 10 randomly selected non-signal locations. Let $\bar{\lambda}^{+}$ and $\bar{\lambda}^{-}$ represent the average of the signal-present responses and signal-absent responses, respectively. The signal present variance, $\hat{\sigma}_{\lambda^{+}}^{2}$, was computed as the sample variance of the signal-present responses. The signal absent variance, $\hat{\sigma}_{\lambda^{-}}^{2}$, was computed at each of the 10 locations and then averaged across location. The resulting estimate of detectability is given by,

$$d'_{bCT} = \frac{\bar{\lambda}^{+} - \bar{\lambda}^{-}}{\sqrt{\frac{1}{2}(\hat{\sigma}^2_{\lambda^+} + \hat{\sigma}^2_{\lambda^-})}}. \quad (1)$$

Detectability is calculated separately for each of the calcium grains. Error in the d' estimation is derived from bootstrapping over the 23 replicated breast CT scans with 1000 resamples (with replication). This represents microcalcification phantom detection performance assessed directly from the breast CT scanner.

4.2.10. Detectability relationship with technique parameters

This study was designed to apply the NPW matched filter model observer to investigate the impact of various technique parameters on microcalcification detectability. The initial parameters studied were detector binning mode (1x1, 2x2), number of projections (250, 500), and dose level (3 mGy, 6 mGy). The V3 (medium size) breast phantom was used for this study with the breast positioned in the typical position near the chest wall.

4.2.11. Detectability relationship with cone angle

This study was designed to apply the NPW matched filter model observer to investigate the relationship between cone angle and detectability when applying the technique parameters used in the clinical trial at UC Davis. The typical clinical protocol is 500 projections with 4 ms pulse width applied in 2x2 binning mode with 60 kV and 0.2 mm Gd filter resulting in 6 mGy dose level. This was setup by inserting the three microcalcification test tube inserts into the V5 breast phantom and positioning it at various locations within the field of view. The V5 (large size) breast phantom was

designed to be positioned near the central ray, however in this study it is setup in three positions separated vertically by 46 mm as depicted in Figure 4.2.

The locations in the field of view correspond to three categories; a small cone angle region positioned near the central ray ($+\mathbf{2}° < \boldsymbol{\theta} < -\mathbf{3}°$), a medium cone angle region ($-\mathbf{4}° < \boldsymbol{\theta} < -\mathbf{9}°$), and a large cone angle region ($-\mathbf{9}° < \boldsymbol{\theta} < -\mathbf{14}°$). Three regions were selected because the height of the microcalcification tube (60 mm) spans one third of the image space (180 mm) and therefore the samples would represent a unique position in each region for comparisons. When the breast is positioned at the medium and large cone angle, the x-rays travel through a greater thickness of the phantom, which would be true for a patient scan as well. The effect of this is not differentiated from the effect of cone angle position, and they are compounded into the detectability evaluation.

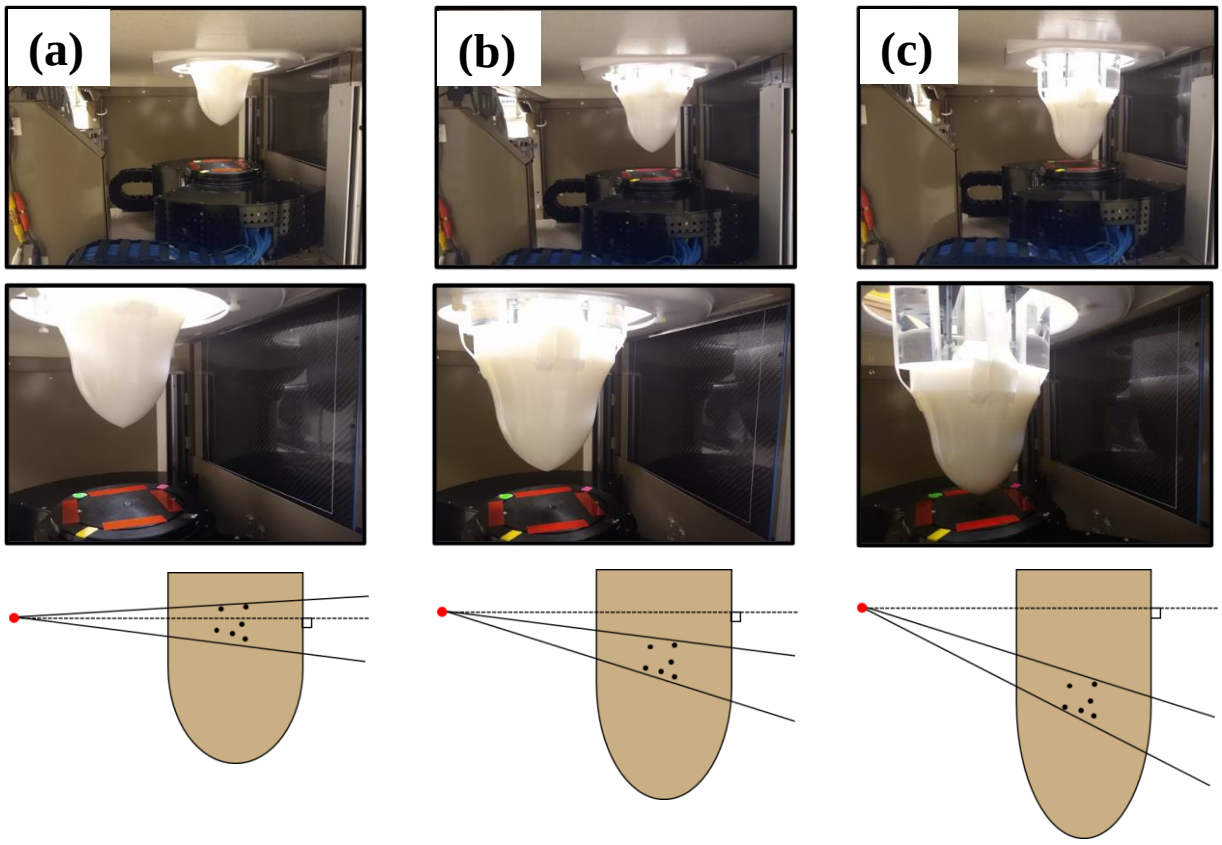

Fig. 4.2 The V5 breast phantom setup on the Doheny gantry system in three positions at (a) small cone angle region (b) medium cone angle region and (c) large cone angle region.

Table 4.1. Summary of the three breast phantom positions and their cone angle regions.

Breast position	Vertical shift	Cone angle region	Initial angle	Final angle
1	0 mm	small cone angle	+2°	-3°
2	46 mm	medium cone angle	-4°	-9°
3	92 mm	large cone angle	-9°	-14°

4.3. Results

4.3.1. Detectability relationship with technique parameters

The results compared between scans of the V3 breast phantom using 1x1 binning mode (75 µm pixels) and 2x2 binning mode (150 µm pixels) at a constant 6 mGy mean glandular dose show that the detector binning mode has a substantial impact on the detectability results (Fig 4.3). Overall, there was a 60% increase in the mean detectability when going from 2x2 binning mode to 1x1 binning mode detector settings.

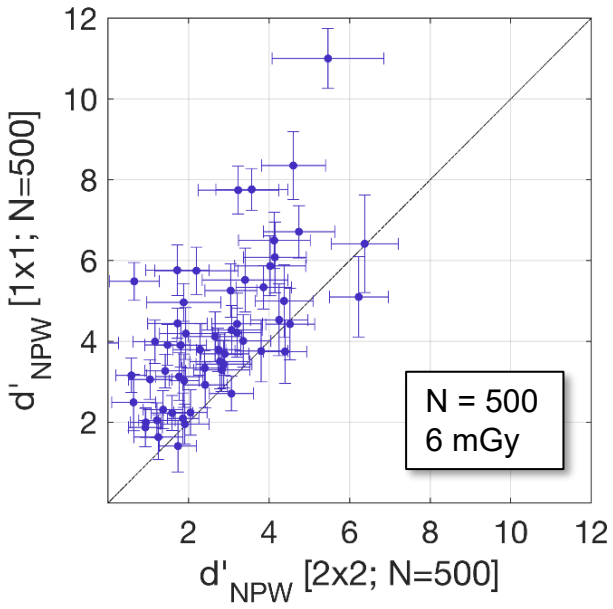

Fig. 4.3. Detectability estimations computed using the breast CT-derived signal templates plotted for 2x2 binning mode (x-axis) and 1x1 binning mode (y-axis) detector settings. Error bars correspond to the 95% confidence interval derived from bootstrapping across the 23 repeat scans.

The detectability compared between scans of the V3 breast phantom with 3 mGy and 6 mGy mean glandular dose (Fig 4.4) both with 1x1 binning mode and 250 projections show that there is substantial difference in the outcome when the dose is reduced by half, which is important because it demonstrates that dose is a limiting factor for this task. Overall, there was a 30% decrease in the mean detectability when going from 6 mGy to 3 mGy mean glandular dose.

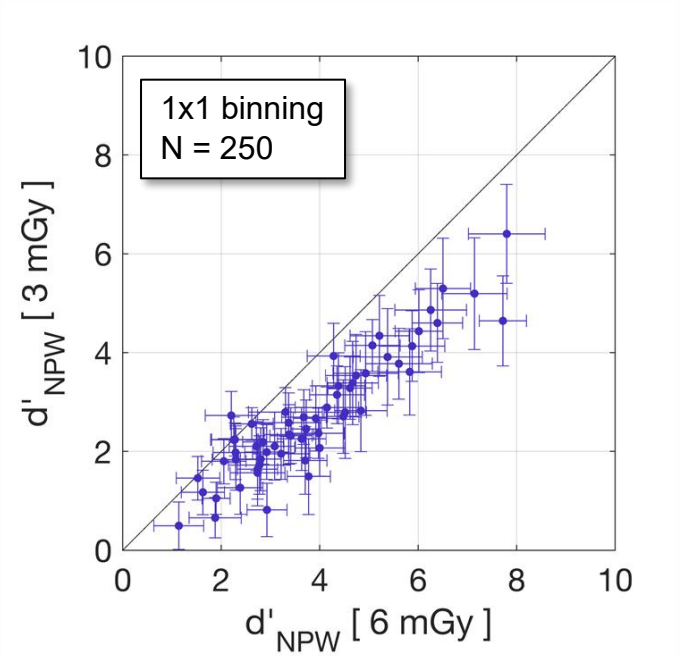

Fig. 4.4. Detectability estimations computed using the breast CT-derived signal templates plotted for 6 mGy (x-axis) and 3 mGy (y-axis) mean glandular dose. Error bars correspond to the 95% confidence interval derived from bootstrapping across the 23 repeat scans.

The detectability compared between scans with 250 projections and 500 projections (Fig 4.5) both with 250 projections and 6 mGy dose shows that there is minimal difference in the outcome when the number of projections is reduced by half, which is significant because it enables faster scan times with less projections. Overall, there was a 7% decrease in the mean detectability when going from 500 to 250 projections.

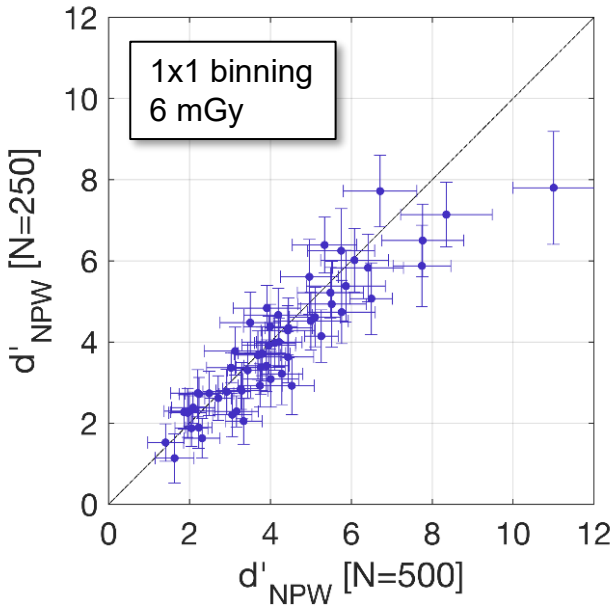

Fig. 4.5. Detectability estimations computed using the breast CT-derived signal templates plotted for 500 projections (x-axis) and 250 projections (y-axis). Error bars correspond to the 95% confidence interval derived from bootstrapping across the 23 repeat scans.

4.3.2. Detectability relationship with cone angle

The phantom experiments for the cone angle study were conducted with the V5 breast phantom to fill the field of view and provide ample movement for phantom re-positioning. These experiments resulted in fewer samples for comparison because only one of the microcalcification tubes could be properly registered between the in-air and the in-phantom scans. This was caused by shifting of the agar material during data collection and the application of 2x2 binning mode for the entire analysis, which resulted in loss of some microcalcification samples. Therefore, 12 microcalcification samples were properly registered for analysis in these studies. The detectability between cone angle positions is demonstrated within the coronal plane (Fig 4.6, Fig 4.7, Fig 4.8), the sagittal plane (Fig 4.9, Fig 4.10, Fig 4.11) , and the axial plane (Fig 4.12, Fig 4.13, Fig 4.14) where each cone angle region is compared to each other. The mean and standard deviation of the detectability for each cone angle region in each plane are reported in Table 4.2. For these comparisons, a paired two-sided t - test $(p < 0.05)$ was applied to determine statistical significance. The detectability in the small cone angle region showed significant differences when compared to the medium and large cone angle regions, however the difference in detectability between the large and medium cone angle regions was not statistically significant.

Table 4.2. Mean detectability and standard deviation of microcalcification lesions across cone angles regions and 3D planes.

	Coronal plane	Sagittal plane	Axial plane
Small cone angle	3.68 ± 2.58	3.06 ± 1.51	2.58 ± 1.59
Medium cone angle	1.86 ± 1.46	2.70 ± 1.59	2.12 ± 1.42
Large cone angle	2.76 ± 1.88	2.52 ± 1.04	1.87 ± 1.00

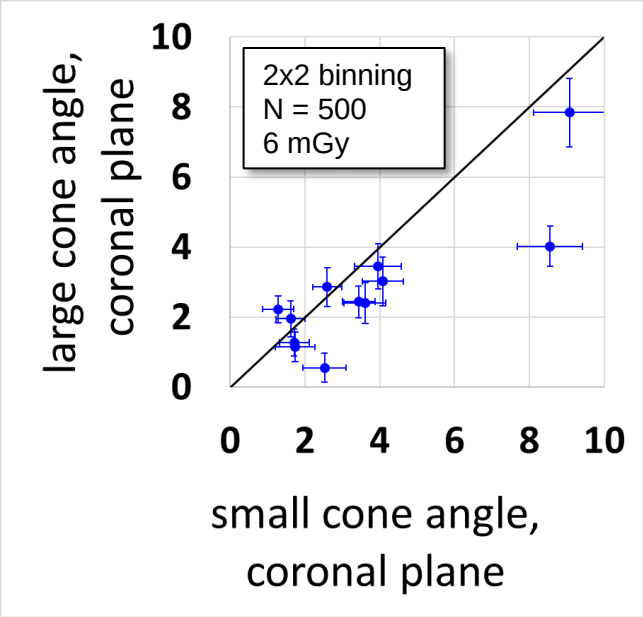

Fig. 4.6. Detectability estimations computed using the breast CT-derived signal templates plotted for small cone angle (x-axis) and large cone angle (y-axis) regions in the coronal plane. Error bars correspond to the 95% confidence interval derived from bootstrapping across the 23 repeat scans.

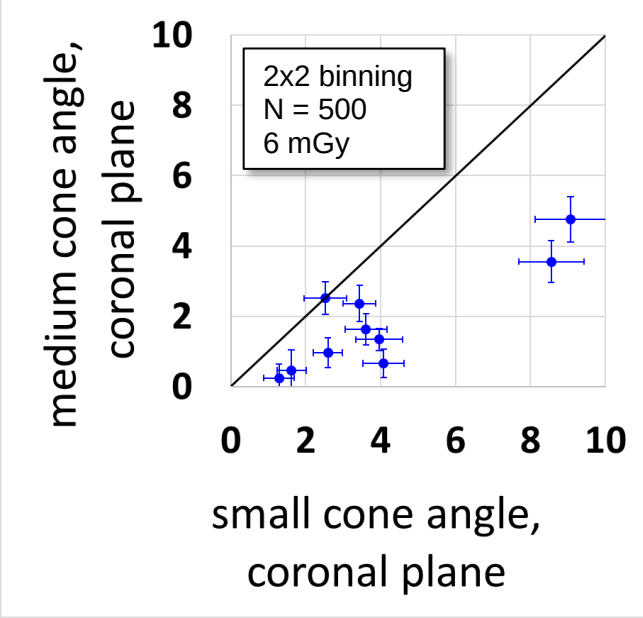

Fig. 4.7. Detectability estimations computed using the breast CT-derived signal templates plotted for small cone angle (x-axis) and medium cone angle (y-axis) regions in the coronal plane. Error bars correspond to the 95% confidence interval derived from bootstrapping across the 23 repeat scans.

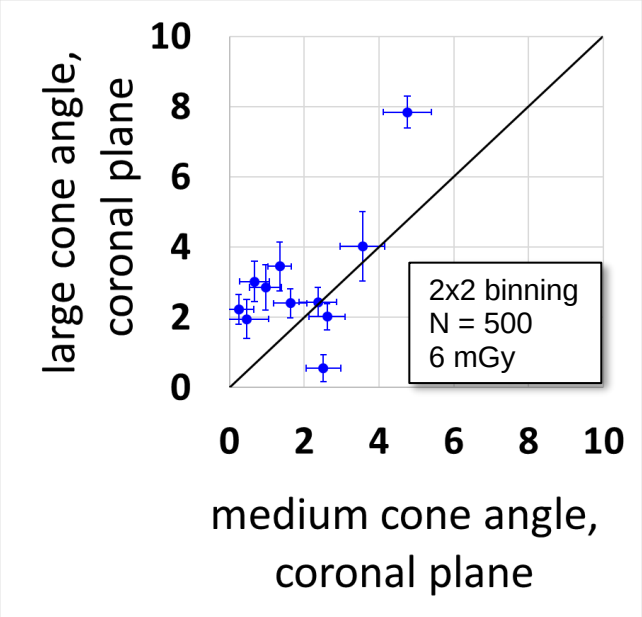

Fig. 4.8. Detectability estimations computed using the breast CT-derived signal templates plotted for medium cone angle (x-axis) and large cone angle (y-axis) regions in the coronal plane. Error bars correspond to the 95% confidence interval derived from bootstrapping across the 23 repeat scans.

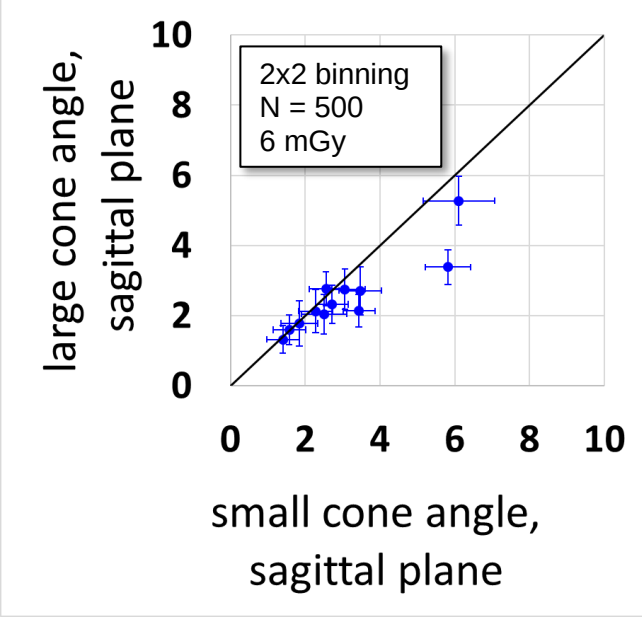

Fig. 4.9. Detectability estimations computed using the breast CT-derived signal templates plotted for small cone angle (x-axis) and large cone angle (y-axis) regions in the sagittal plane. Error bars correspond to the 95% confidence interval derived from bootstrapping across the 23 repeat scans.

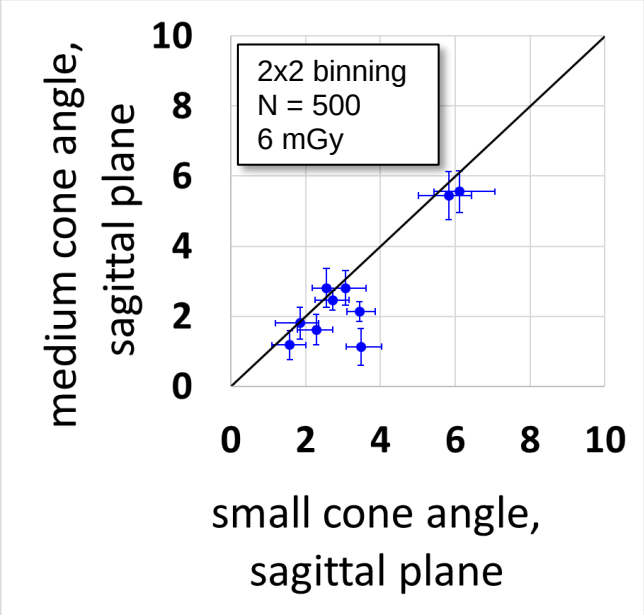

Fig. 4.10 Detectability estimations computed using the breast CT-derived signal templates plotted for small cone angle (x-axis) and medium cone angle (y-axis) regions in the sagittal plane. Error bars correspond to the 95% confidence interval derived from bootstrapping across the 23 repeat scans.

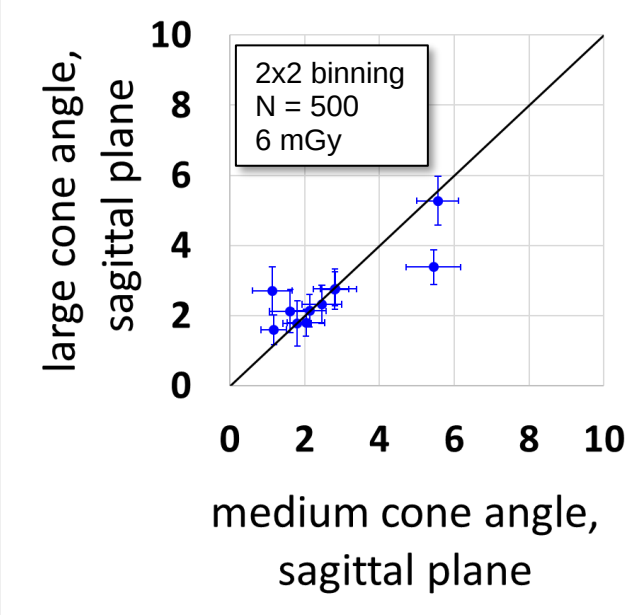

Fig. 4.11. Detectability estimations computed using the breast CT-derived signal templates plotted for medium cone angle (x-axis) and large cone angle (y-axis) regions in the sagittal plane. Error bars correspond to the 95% confidence interval derived from bootstrapping across the 23 repeat scans.

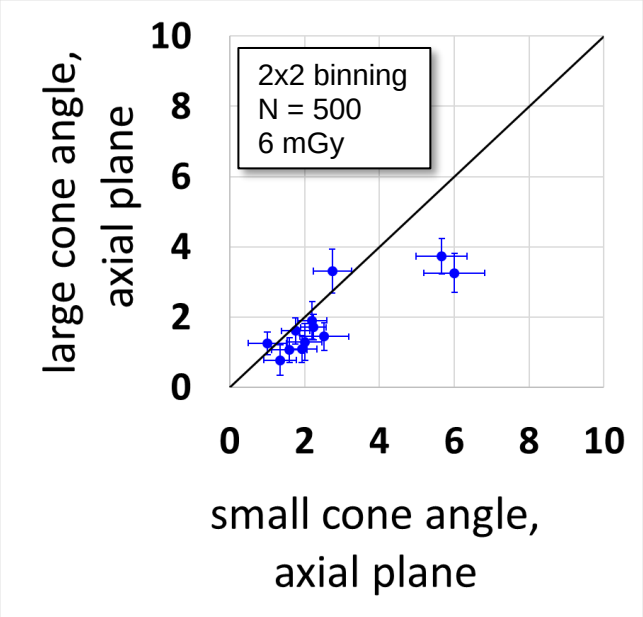

Fig. 4.12. Detectability estimations computed using the breast CT-derived signal templates plotted for small cone angle (x-axis) and large cone angle (y-axis) regions in the axial plane. Error bars correspond to the 95% confidence interval derived from bootstrapping across the 23 repeat scans.

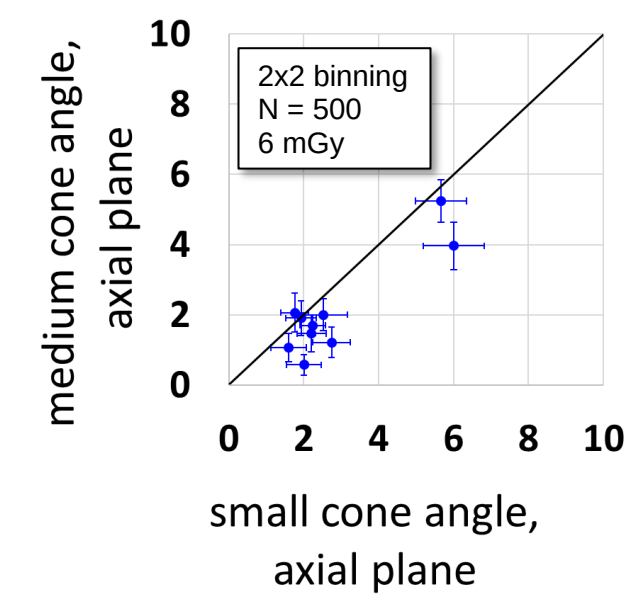

Fig. 4.13. Detectability estimations computed using the breast CT-derived signal templates plotted for small cone angle (x-axis) and medium cone angle (y-axis) regions in the axial plane. Error bars correspond to the 95% confidence interval derived from bootstrapping across the 23 repeat scans.

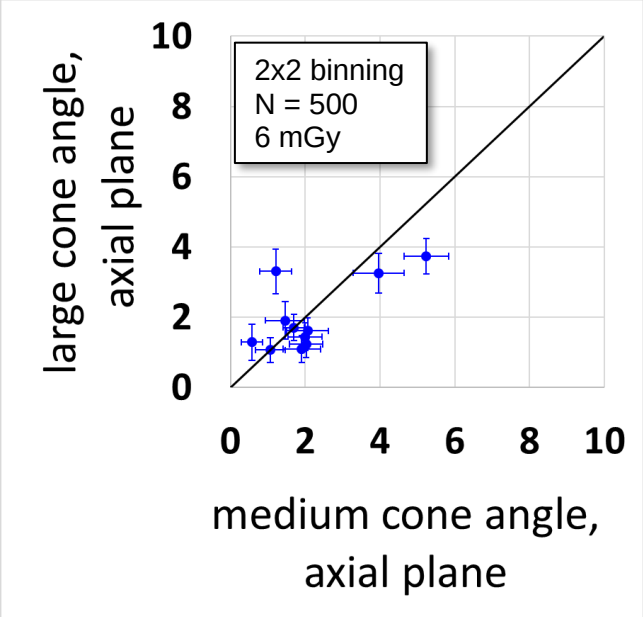

Fig. 4.14. Detectability estimations computed using the breast CT-derived signal templates plotted for small cone angle (x-axis) and medium cone angle (y-axis) regions in the axial plane. Error bars correspond to the 95% confidence interval derived from bootstrapping across the 23 repeat scans.

4.3.3. Detectability relationship with plane of detection

The detectability within the regions of small cone angle (Fig 4.15), medium cone angle (Fig 4.16), and large cone angle (Fig 4.17) were demonstrated within 3D space where two of the planes (coronal and axial) were compared with each other. There was a 30% decrease in the mean detectability when going from the coronal plane to the axial plane for both the small cone angle and large cone angle regions, with statistical significance determined by a paired two-sided t-test ($p < 0.05$). There was no significant difference in detectability between planes in the medium cone angle region (Fig 4.16)

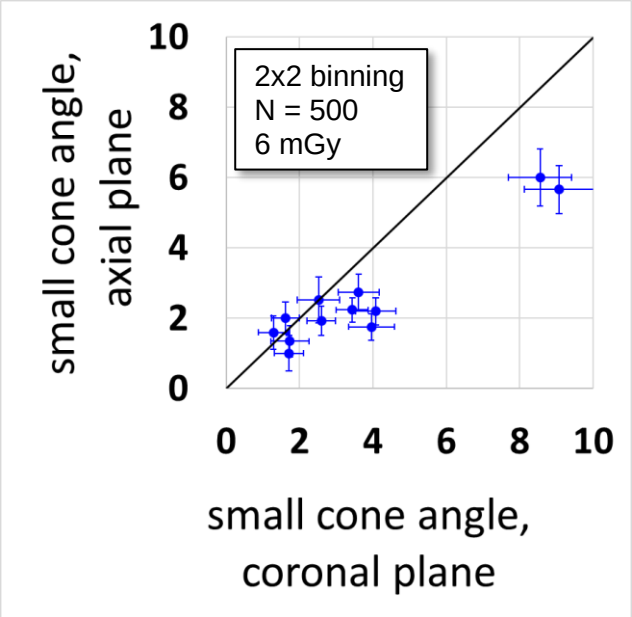

Fig. 4.15. Detectability estimations computed using the breast CT-derived signal templates plotted for coronal plane (x-axis) and axial plane (y-axis) in the small cone angle region. Error bars correspond to the 95% confidence interval derived from bootstrapping across the 23 repeat scans.

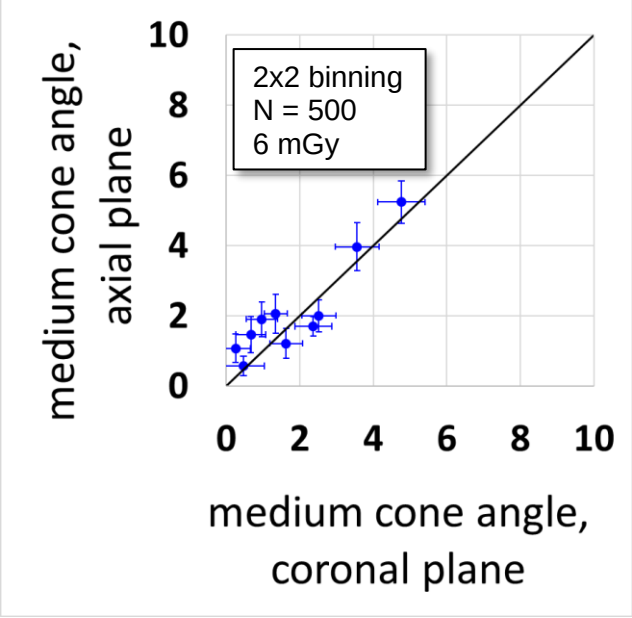

Fig. 4.16. Detectability estimations computed using the breast CT-derived signal templates plotted for the coronal plane (x-axis) and axial plane (y-axis) in the medium cone angle region. Error bars correspond to the 95% confidence interval derived from bootstrapping across the 23 repeat scans.

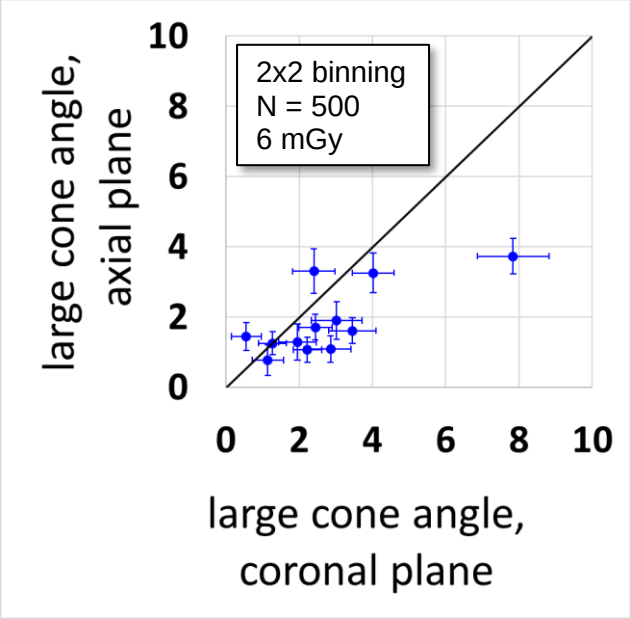

Fig. 4.17. Detectability estimations computed using the breast CT-derived signal templates plotted for the coronal plane (x-axis) and axial plane (y-axis) in the medium cone angle region. Error bars correspond to the 95% confidence interval derived from bootstrapping across the 23 repeat scans.

4.4. Discussion

The technique parameters investigated demonstrated that detectability of simulated microcalcifications is improved with smaller pixel size (1x1 binning mode, 75 µm pixel) and higher dose (6 mGy) when compared to larger pixel size (2x2 binning mode, 150 µm pixel) and lower dose (3 mGy). However, the number of projections (N = 250 or N = 500) did not affect the detectability significantly. In the cone angle studies, the detectability decreased going from small to medium cone angle regions and from small to large cone angle regions but was not significantly affected going from medium to large cone angle regions. The coronal plane demonstrated significant differences in detectability across different cone angle regions, whereas the sagittal plane and axial plane demonstrated moderate differences across cone angle regions (Table 4.1). These results demonstrate that detectability of microcalcifications is reduced by applying medium

and large cone angles, which suggests that the six-source collimated configuration with small cone angles (described in Chapter 3) could offer a better cone beam CT system design for this specific lesion detection task.

Based on previous studies[95,100] that characterized the length of breast tissue for a cohort of patients with clinical bCT, it would be expected that the loss in detectability across cone angle regions could affect all patients with microcalcification lesions. This is because the length of all breast size categories reported (V1, V2, V3, V4, V5, V6) encompasses the medium cone angle region, and the length of most breast size categories (V2, V3, V4, V5, V6) reported encompasses the large cone angle region of this study. This is under the assumption that the reported trend across cone angle regions is independent from the breast volume, which has yet to be proven experimentally.

4.5. Conclusion

The NPW matched filter model provided a useful tool for evaluating the detectability of microcalcification lesions in phantom studies for various technique parameters and for various locations within the field of view for breast CT. Future studies will include investigation of more breast phantom sizes and dose levels in the 1x1 detector binning mode.

Chapter 5: Conclusions

This dissertation shows the potential of the novel MXA technology to improve DBT and CBCT systems with three main projects in the field of breast cancer imaging. The first project included the design and characterization of a novel x-ray tube with metrics including x-ray spectra, tube output, half value layer, focal spot, and tube modulation. The prototype demonstrated operating characteristics consistent with x-ray tubes required for stationary source DBT and initial tomosynthesis datasets were reconstructed. Future prototype studies will utilize MXA for DBT imaging and quantification using the MQSA phantom and other high contrast objects.

The second project included physical simulations and Monte Carlo simulations to investigate the potential of this novel x-ray tube for unique multisource configurations in CBCT. The collimated six source configuration offers substantial reduction in scatter and dose with improved image quality when compared to traditional one source CBCT. The multisource configurations could be realized into physical systems with the integration of a prototype MXA.

The third project included the development of a specialized lesion phantom for dedicated bCT and a mathematical observer to evaluate microcalcification detectability. Several technique parameters were investigated, and it was found that dose level and pixel size impact detectability, while the number of projections did not impact detectability. This demonstrates important outcomes for the optimization of dedicated breast CT for screening because microcalcifications are necessary for early detection. The impact of the cone angle region and the plane of detection on the detectability of microcalcifications was quantified and suggests that the collimated six source configuration with only small cone angle regions could be a better system design to eliminate the effects of medium and large cone angles. The application of the collimated six source

configuration to breast CT would also substantially reduce the scatter contamination, which would also improve the detectability of microcalcifications. Continuous investigation will be conducted on the effects of breast size and dose level to reach equal detectability across breast sizes.

References

1. DeSantis CE, Ma J, Gaudet MM, et al. Breast cancer statistics, 2019. *CA Cancer J Clin*. 2019;69(6):438-451. doi:10.3322/caac.21583

2. Kemp Jacobsen K, O'Meara ES, Key D, et al. Comparing sensitivity and specificity of screening mammography in the United States and Denmark. *Int J cancer*. 2015;137(9):2198-2207. doi:10.1002/ijc.29593

3. Neculaes VB, Edic PM, Frontera M, Caiafa A, Wang G, De Man B. Multisource X-Ray and CT: Lessons learned and future outlook. *IEEE Access*. 2014;2:1568-1585. doi:10.1109/ACCESS.2014.2363949

4. Siemens SOMATOM Dual Source CT Scanners. *https://www.siemens-healthineers.com/en-us/computed-tomography/dual-source-ct*.

5. Boyd DP, Couch JL, Napel SA, et al. High-Speed, Multi-Slice, X-Ray Computed Tomography. In: Nalcioglu O, ed. *Physics and Engineering in Medical Imaging*. Vol 0372. SPIE; 1982:139-150. doi:10.1117/12.934506

6. Handbook of Materials and Techniques for Vacuum Devices | Walter Kohl | American Institute of Physics | Springer.

7. Zhu W, ed. *Vacuum Microelectronics*. New York, USA: John Wiley & Sons, Inc.; 2001. doi:10.1002/0471224332

8. Neculaes VB, Caiafa A, Cao Y, et al. Multisource inverse-geometry CT. Part II. X-ray source design and prototype. *Med Phys*. 2016;43(8Part1):4617-4627. doi:10.1118/1.4954847

9. Calliste J, Wu G, Laganis PE, et al. Second generation stationary digital breast tomosynthesis system with faster scan time and wider angular span. *Med Phys*. 2017;44(9):4482-4495. doi:10.1002/mp.12393

10. Kleint C. On the early history of field emission including attempts of tunneling spectroscopy. *Prog Surf Sci*. 1993;42(1-4):101-115. doi:10.1016/0079-6816(93)90064-3

11. Sechopoulos I. A review of breast tomosynthesis. Part I. The image acquisition process. *Med Phys*. 2013;40(1):014301. doi:10.1118/1.4770279

12. Behling R. *X-RAY TUBES DEVELOPMENT-IOMP HISTORY OF MEDICAL PHYSICS*. Vol 1.; 2018. http://mpijournal.org/history.aspx

13. Boone JM, Becker AE, Hernandez AM, Dobbins JT, Schwoebelc P. Multi-x-ray source array for stationary tomosynthesisor multi-cone angle cone beam CT. In: Bosmans H, Chen G-H, Gilat Schmidt T, eds. *Medical Imaging 2019: Physics of Medical Imaging*. Vol 10948. SPIE; 2019:29. doi:10.1117/12.2512959

14. Becker AE, Hernandez AM, Schwoebel PR, Boone JM. Cone beam CT multisource configurations: evaluating image quality, scatter, and dose using phantom imaging and Monte Carlo simulations. *Phys Med Biol*. October 2020. doi:10.1088/1361-6560/abc306

15. Becker AE, Hernandez AM, Schwoebel P, Boone JM. Multisource x-ray system for artifact reduction in dedicated breast CT. In: Krupinski EA, ed. *14th International Workshop on Breast Imaging (IWBI 2018)*. Vol 10718. SPIE; 2018:19. doi:10.1117/12.2317846

16. Becker AE, Hernandez AM, Boone JM, Schwoebel PR. A prototype multi-x-ray-source array (MXA) for digital breast tomosynthesis. *Phys Med Biol*. October 2020. doi:10.1088/1361-6560/abc305

17. Robb RA. The Dynamic Spatial Reconstructor: An X-Ray Video-Fluoroscopic CT Scanner for Dynamic Volume Imaging of Moving Organs. *IEEE Trans Med Imaging*. 1982;1(1):22-33. doi:10.1109/TMI.1982.4307545

18. Fahrig R, Dixon R, Payne T, Morin RL, Ganguly A, Strobel N. Dose and image quality for a cone-beam C-arm CT system. *Med Phys*. 2006;33(12):4541-4550. doi:10.1118/1.2370508

19. Miracle AC, Mukherji SK. Conebeam CT of the Head and Neck, Part 2: Clinical Applications. *Am J Neuroradiol*. 2009;30(7):1285-1292. doi:10.3174/ajnr.A1654

20. Jaffray D, Siewerdsen J, Gospodarowicz M. Radiation Oncology. In: *Image-Guided Interventions*. Boston, MA: Springer US; 2008:501-529. doi:10.1007/978-0-387-73858-1_17

21. Jaffray DA, Siewerdsen JH, Wong JW, Martinez AA. Flat-panel cone-beam computed tomography for image-guided radiation therapy. *Int J Radiat Oncol*. 2002;53(5):1337-1349. doi:10.1016/S0360-3016(02)02884-5

22. Posadzy M, Desimpel J, Vanhoenacker F. Cone beam CT of the musculoskeletal system: clinical applications. *Insights Imaging*. 2018;9(1):35-45. doi:10.1007/s13244-017-0582-1

23. Gazi PM, Yang K, Burkett GW, Aminololama-Shakeri S, Seibert J, Boone JM. Evolution of spatial resolution in breast CT at UC Davis. *Med Phys*. 2015;42(4):1973-1981. doi:10.1118/1.4915079

24. Lindfors KK, Boone JM, Nelson TR, Yang K, Kwan ALC, Miller DF. Dedicated Breast CT: Initial Clinical Experience. *Radiology*. 2008;246(3):725-733. doi:10.1148/radiol.2463070410

25. Verdun FR, Racine D, Ott JG, et al. Image quality in CT: From physical measurements to model observers. *Phys Medica*. 2015;31(8):823-843. doi:10.1016/J.EJMP.2015.08.007

26. Barrett HH, Yao J, Rolland JP, Myers KJ. Model observers for assessment of image quality. *Proc Natl Acad Sci U S A*. 1993;90(21):9758-9765. http://www.ncbi.nlm.nih.gov/pubmed/8234311. Accessed February 12, 2019.

27. Zhang Y, Leng S, Yu L, Carter RE, McCollough CH. Correlation between human and model observer performance for discrimination task in CT. *Phys Med Biol*. 2014;59(13):3389-3404. doi:10.1088/0031-9155/59/13/3389

28. Tirada N, Li G, Dreizin D, et al. Digital breast tomosynthesis: Physics, artifacts, and quality control considerations. *Radiographics*. 2019;39(2):413-426. doi:10.1148/rg.2019180046

29. Horvat J V., Keating DM, Rodrigues-Duarte H, Morris EA, Mango VL. Calcifications at digital breast tomosynthesis: Imaging features and biopsy techniques. *Radiographics*. 2019;39(2):307-318. doi:10.1148/rg.2019180124

30. Smith AE. *Design Considerations in Optimizing a Breast Tomosynthesis System*.; 2011. https://hologic.tecnoimagen.cl/wp-content/uploads/2020/11/Optimisation-Breast-Tomo-System-Andrew-Smith-WP-00046-Rev002-1.pdf.

31. Kopans DB. Digital breast tomosynthesis from concept to clinical care. *Am J Roentgenol*. 2014;202(2):299-308. doi:10.2214/AJR.13.11520

32. Shrestha S, Vedantham S, Karellas A. Towards standardization of x-ray beam filters in digital

mammography and digital breast tomosynthesis: Monte Carlo simulations and analytical modelling. *Phys Med Biol*. 2017;62(5):1969-1993. doi:10.1088/1361-6560/aa58c8

33. The Essential Physics of Medical Imaging, 4th Edition, JT Bushberg, JA Seibert, EM Liedholdt, JM Boone, Wolters Kluwer, Philadelphia, PA 2021

34. Godfrey DJ, Rader A, Dobbins III JT. Practical strategies for the clinical implementation of matrix inversion tomosynthesis (MITS). In: Yaffe MJ, Antonuk LE, eds. *Medical Imaging 2003: Physics of Medical Imaging*. Vol 5030. SPIE; 2003:379. doi:10.1117/12.480352

35. Zhou W, Lu J, Zhou O, Chen Y. Evaluation of Back Projection Methods for Breast Tomosynthesis Image Reconstruction. *J Digit Imaging*. 2015;28(3):338-345. doi:10.1007/s10278-014-9736-6

36. Godfrey DJ, Page McAdams H, Dobbins JT. The effect of averaging adjacent planes for artifact reduction in matrix inversion tomosynthesis. *Med Phys*. 2013;40(2). doi:10.1118/1.4773891

37. Tuy HK. An Inversion Formula for Cone-Beam Reconstruction. *SIAM J Appl Math*. 1983;43(3):546-552. doi:10.1137/0143035

38. Ozaki Y, Watanabe H, Nomura Y, Honda E, Sumi Y, Kurabayashi T. Location dependency of the spatial resolution of cone beam computed tomography for dental use. *Oral Surg Oral Med Oral Pathol Oral Radiol*. 2013;116(5):648-655. doi:10.1016/J.OOOO.2013.07.009

39. Endo M, Tsunoo T, Nakamori N, Yoshida K. Effect of scattered radiation on image noise in cone beam CT. *Med Phys*. 2001;28(4):469-474. doi:10.1118/1.1357457

40. Scarfe WC, Farman AG. What is Cone-Beam CT and How Does it Work? *Dent Clin North Am*. 2008;52(4):707-730. doi:https://doi.org/10.1016/j.cden.2008.05.005

41. Yoo S, Yin FF. Dosimetric feasibility of cone-beam CT-based treatment planning compared to CT-based treatment planning. *Int J Radiat Oncol Biol Phys*. 2006. doi:10.1016/j.ijrobp.2006.08.031

42. Parsa A, Ibrahim N, Hassan B, van der Stelt P, Wismeijer D. Bone quality evaluation at dental implant site using multislice CT, micro-CT, and cone beam CT. *Clin Oral Implants Res*. 2015;26(1):e1-e7. doi:10.1111/clr.12315

43. Demehri S, Muhit A, Zbijewski W, et al. Assessment of image quality in soft tissue and bone visualization tasks for a dedicated extremity cone-beam CT system. *Eur Radiol*. 2015;25(6):1742-1751. doi:10.1007/s00330-014-3546-6

44. Faccioli N, Foti G, Barillari M, Atzei A, Mucelli RP. Finger fractures imaging: accuracy of cone-beam computed tomography and multislice computed tomography. *Skeletal Radiol*. 2010;39(11):1087-1095. doi:10.1007/s00256-010-0911-7

45. Neubauer J, Benndorf M, Reidelbach C, et al. Comparison of Diagnostic Accuracy of Radiation Dose-Equivalent Radiography, Multidetector Computed Tomography and Cone Beam Computed Tomography for Fractures of Adult Cadaveric Wrists. Woloschak GE, ed. *PLoS One*. 2016;11(10):e0164859. doi:10.1371/journal.pone.0164859

46. Wood R, Sun Z, Chaudhry J, et al. Factors affecting the accuracy of buccal alveolar bone height measurements from cone-beam computed tomography images. *Am J Orthod Dentofac Orthop*. 2013;143(3):353-363. doi:10.1016/J.AJODO.2012.10.019

47. Gang GJ, Zbijewski W, Mahesh M, et al. Image quality and dose for a multisource cone-beam CT extremity scanner. *Med Phys*. 2018;45(1):144-155. doi:10.1002/mp.12659

48. Gilat Schmidt T. Preliminary feasibility of dedicated breast CT with an inverse geometry. In: Samei E, Hsieh J, eds. Vol 7258. International Society for Optics and Photonics; 2009:72582Y. doi:10.1117/12.811772

49. Schmidt TG, Fahrig R, Pelc NJ, Solomon EG. An inverse-geometry volumetric CT system with a large-area scanned source: A feasibility study. *Med Phys*. 2004;31(9):2623-2627. doi:10.1118/1.1786171

50. Neculaes VB, Caiafa A, Cao Y, et al. Multisource inverse-geometry CT. Part II. X-ray source design and prototype. *Med Phys*. 2016;43(8):4617-4627. doi:10.1118/1.4954847

51. Baek J, Pelc NJ. A new method to combine 3D reconstruction volumes for multiple parallel circular cone beam orbits. *Med Phys*. 2010;37(10):5351-5360. doi:10.1118/1.3484058

52. Han C, Baek J. Multi-pass approach to reduce cone-beam artifacts in a circular orbit cone-beam CT system. *Opt Express*. 2019;27(7):10108. doi:10.1364/OE.27.010108

53. Yin Zhye , De Man Bruno PJ. 3D Analytic Cone-Beam Reconstruction for Multiaxial CT Acquisitions. *Int J Biomed Imaging*. 2009.

54. Fu J, Fan D. Volumetric Reconstruction Technique for Multiple Parallel Circular Orbits CT. Advances in Engineering Research. April 2015. https://doi.org/10.2991/meic-15.2015.33

55. Shah JP, Mann SD, McKinley RL, Tornai MP. Three dimensional dose distribution comparison of simple and complex acquisition trajectories in dedicated breast CT. *Med Phys.* 2015;42(8):4497-4510. doi:10.1118/1.4923169

56. Vedantham S, Shi L, Karellas A, Noo F. Dedicated breast CT: radiation dose for circle-plus-line trajectory. *Med Phys*. 2012;39(3):1530-1541. doi:10.1118/1.3688197

57. Kachelrieß, M., Knaup, M. & Kalender, W. A. Multithreaded cardiac CT. Med. Phys. 33, 2435–2447 (2006).. https://doi.org/10.1118/1.2207236

58. Zhao J, Jin Y, Lu Y, Wang G. A Filtered backprojection algorithm for triple-source helical cone-beam CT. *IEEE Trans Med Imaging*. 2009;28(3):384-393. doi:10.1109/TMI.2008.2004817

59. Chen Y, Xi Y, Zhao J. A SEMI-stationary CT system. In: *2014 IEEE 11th International Symposium on Biomedical Imaging, ISBI 2014*. Institute of Electrical and Electronics Engineers Inc.; 2014:1099-1102. doi:10.1109/isbi.2014.6868066

60. Chen Y, Xi Y, Zhao J. A stationary computed tomography system with cylindrically distributed sources and detectors. *J Xray Sci Technol*. 2014;22(6):707-725. doi:10.3233/XST-140456

61. Siewerdsen JH, Moseley DJ, Bakhtiar B, Richard S, Jaffray DA. The influence of antiscatter grids on soft-tissue detectability in cone-beam computed tomography with flat-panel detectors. *Med Phys*. 2004;31(12):3506-3520. doi:10.1118/1.1819789

62. Poludniowski G, Evans PM, Hansen VN, Webb S. An efficient Monte Carlo-based algorithm for scatter correction in keV cone-beam CT. *Phys Med Biol*. 2009;54(12):3847-3864. doi:10.1088/0031-9155/54/12/016

63. Chen Y, Song Y, Ma J, Zhao J. Optimization-based scatter estimation using primary modulation for computed tomography. *Med Phys*. 2016;43(8):4753-4767. doi:10.1118/1.4958680

64. Siewerdsen JH, Daly MJ, Bakhtiar B, et al. A simple, direct method for x-ray scatter estimation and correction in digital radiography and cone-beam CT. *Med Phys*. 2005;33(1):187-197. doi:10.1118/1.2148916

65. Zhu L, Xie Y, Wang J, Xing L. Scatter correction for cone-beam CT in radiation therapy. *Med Phys*. 2009;36(6Part1):2258-2268. doi:10.1118/1.3130047

66. Gong H, Li B, Jia X, Cao G. Physics Model-Based Scatter Correction in Multi-Source Interior Computed Tomography. *IEEE Trans Med Imaging*. 2018;37(2):349-360. doi:10.1109/TMI.2017.2741259

67. Ghazi P, Hernandez AM, Abbey C, Yang K, Boone JM. Shading artifact correction in breast CT using an interleaved deep learning segmentation and maximum likelihood polynomial fitting approach. *Med Phys*. 2019;46(8):mp.13599. doi:10.1002/mp.13599

68. Feldkamp LA, Davis LC, Kress JW. Practical cone-beam algorithm. *J Opt Soc Am A*. 1984;1(6):612-619. doi:10.1364/JOSAA.1.000612

69. Siewerdsen JH, Uneri A, Hernandez AM, et al. Cone-Beam CT Dose and Imaging Performance Evaluation 5 with a Modular, Multi-Purpose Phantom. *Med Phys*. 2019. doi: 10.1002/mp.13952

70. Bartolac S, Clackdoyle R, Noo F, Siewerdsen J, Moseley D, Jaffray D. A local shift-variant Fourier model and experimental validation of circular cone-beam computed tomography artifacts. *Med Phys*. 2009;36(2):500-512. doi:doi:10.1118/1.3062875

71. Baek J, Pelc NJ. Local and global 3D noise power spectrum in cone-beam CT system with FDK reconstruction. *Med Phys*. 2011;38(4):2122-2131. doi:10.1118/1.3556590

72. MCNP X. Monte Carlo Team, MCNP—a general purpose Monte Carlo N-particle transport code, version 5. 2003:LA-UR-03-1987, Los Alamos National Laboratory.

73. Hernandez AM, Boone JM. Tungsten anode spectral model using interpolating cubic splines: unfiltered x-ray spectra from 20 kV to 640 kV. *Med Phys*. 2014;41(4):042101. doi:10.1118/1.4866216

74. Smans K, Zoetelief J, Verbrugge B, et al. Simulation of image detectors in radiology for determination of scatter-to-primary ratios using Monte Carlo radiation transport code MCNP/MCNPX. *Med Phys*. 2010;37(5):2082-2091. doi:10.1118/1.3377773

75. Zunzunegui RG, Chung MA, Oruwari J, Golding D, Marchant DJ, Cady B. Casting-Type Calcifications With Invasion and High-Grade Ductal Carcinoma In Situ. *Arch Surg*. 2003;138(5):537. doi:10.1001/archsurg.138.5.537

76. Rauch GM, Hobbs BP, Kuerer HM, et al. Microcalcifications in 1657 Patients with Pure Ductal Carcinoma in Situ of the Breast: Correlation with Clinical, Histopathologic, Biologic Features, and Local Recurrence. *Ann Surg Oncol*. 2016;23(2):482-489. doi:10.1245/s10434-015-4876-6

77. Hofvind S, Iversen BF, Eriksen L, Styr BM, Kjellevold K, Kurz KD. Mammographic morphology and distribution of calcifications in ductal carcinoma *in situ* diagnosed in organized screening. *Acta radiol*. 2011;52(5):481-487. doi:10.1258/ar.2011.100357

78. Barreau B, Mascarel I de, Feuga C, et al. Mammography of ductal carcinoma in situ of the breast: Review of 909 cases with radiographic–pathologic correlations. *Eur J Radiol*. 2005;54(1):55-61. doi:10.1016/J.EJRAD.2004.11.019

79. Holland R, Hendriks JH. Microcalcifications associated with ductal carcinoma in situ: mammographic-pathologic correlation. *Semin Diagn Pathol*. 1994;11(3):181-192. http://www.ncbi.nlm.nih.gov/pubmed/7831529. Accessed February 21, 2019.

80. Aminololama-Shakeri S, Abbey CK, Gazi P, et al. Differentiation of ductal carcinoma in-situ from

benign micro-calcifications by dedicated breast computed tomography. *Eur J Radiol*. 2016;85(1):297-303. doi:https://doi.org/10.1016/j.ejrad.2015.09.020

81. Prionas ND, Lindfors KK, Ray S, et al. Contrast-enhanced Dedicated Breast CT: Initial Clinical Experience. *Radiology*. 2010;256(3):714-723. doi:10.1148/radiol.10092311

82. Gong X, Vedula AA, Glick SJ. Microcalcification detection using cone-beam CT mammography with a flat-panel imager. *Phys Med Biol*. 2004;49(11):2183-2195. doi:10.1088/0031-9155/49/11/005

83. Sanchez AA, Sidky EY, Pan X. Task-based optimization of dedicated breast CT via Hotelling observer metrics. *Med Phys*. 2014;41(10):101917. doi:10.1118/1.4896099

84. Han M, Kim B, Baek J. Human and model observer performance for lesion detection in breast cone beam CT images with the FDK reconstruction. *PLoS One*. 2018;13(3):e0194408. doi:10.1371/journal.pone.0194408

85. Lai C-J, Shaw CC, Chen L, et al. Visibility of microcalcification in cone beam breast CT: Effects of x-ray tube voltage and radiation dose. *Med Phys*. 2007;34(7):2995-3004. doi:10.1118/1.2745921

86. Packard NJ, Abbey CK, Yang K, Boone JM. Effect of slice thickness on detectability in breast CT using a prewhitened matched filter and simulated mass lesions. *Med Phys*. 2012;39(4):1818-1830. doi:10.1118/1.3692176

87. Chen L, Boone JM, Abbey CK, et al. Simulated lesion, human observer performance comparison between thin-section dedicated breast CT images versus computed thick-section simulated projection images of the breast. *Phys Med Biol*. 2015;60(8):3347-3358. doi:10.1088/0031-9155/60/8/3347

88. Myers KJ, Barrett HH, Borgstrom MC, Patton DD, Seeley GW. *Effect of Noise Correlation on Detectability of Disk Signals in Medical Imaging*. Vol 2.; 1985. doi: 10.1364/josaa.2.001752

89. Cho HM, Ding H, Barber WC, Iwanczyk JS, Molloi S. Microcalcification detectability using a bench-top prototype photon-counting breast CT based on a Si strip detector. *Med Phys*. 2015;42(7):4401-4410. doi:10.1118/1.4922680

90. Henrot P, Leroux A, Barlier C, Génin P. Breast microcalcifications: The lesions in anatomical pathology. *Diagn Interv Imaging*. 2014;95(2):141-152. doi:10.1016/j.diii.2013.12.011

91. Barth V, Franz ED, Schöll A. Microcalcifications in mammary glands. *Naturwissenschaften*. 1977;64(5):278-279. doi:10.1007/BF00438314

92. Sathyavathi R, Saha A, Soares JS, et al. Raman spectroscopic sensing of carbonate intercalation in breast microcalcifications at stereotactic biopsy. *Sci Rep*. 2015;5. doi:10.1038/srep09907

93. Hassler O. Microradiographic investigations of calcifications of the female breast. *Cancer*. 1969;23(5):1103-1109. doi:10.1002/1097-0142(196905)23:5<1103::AID-CNCR2820230514>3.0.CO;2-7

94. Willekens I, Van de Casteele E, Buls N, et al. High-resolution 3D micro-CT imaging of breast microcalcifications: A preliminary analysis. *BMC Cancer*. 2014;14(1). doi:10.1186/1471-2407-14-9

95. Hernandez AM, Boone JM. Average glandular dose coefficients for pendant-geometry breast CT using realistic breast phantoms. *Med Phys*. 2017;44(10):5096-5105. doi:doi:10.1002/mp.12477

96. Hernandez A, Becker A, Lyu SH, Abbey C, Boone J. High-resolution μCT imaging for characterizing microcalcification detection performance in breast CT. [Submitted to *J Med Imaging*. 2021]

97. Hernandez AM, Abbey CK, Ghazi P, Burkett G, Boone JM. Effects of kV, filtration, dose and object size on soft tissue and iodine contrast in dedicated breast CT. *Med Phys*. March 2020. doi:10.1002/mp.14159

98. Otsu N. THRESHOLD SELECTION METHOD FROM GRAY-LEVEL HISTOGRAMS. *IEEE Trans Syst Man Cybern*. 1979;SMC-9(1):62-66. doi:10.1109/tsmc.1979.4310076

99. Hernandez AM, Becker AE, Lyu SH, Abbey CK, Boone JM. High resolution microcalcification signal profiles for dedicated breast CT. In: Bosmans H, Chen G-H, eds. *Medical Imaging 2020: Physics of Medical Imaging*. Vol 2020. SPIE; 2020:21. doi:10.1117/12.2549872

100. Hernandez AM, Becker AE, Boone JM. Updated breast CT dose coefficients (DgN_{CT}) using patient-derived breast shapes and heterogenous fibroglandular distributions. *Med Phys*. January 2019. doi:10.1002/mp.13391